Research in Astronomy and Astrophysics, 24:095003 (23pp), 2024 September https://doi.org/10.1088/1674-4527/ad6c95

On the Relation Between Symmetry of Radio Galaxies and Their Physical Parameters

Mohsen Javaherian, Halime Miraghaei, and Hooman Moradpour
Research Institute for Astronomy and Astrophysics of Maragha (RIAAM), University of Maragheh, P.O. Box 55136-553, Maragheh, Iran; javaherian@maragheh.ac.ir
Received 2024 March 6; revised 2024 July 20; accepted 2024 August 6; published 2024 August 28

Abstract

Gravity as a fundamental force plays a dominant role in the formation and evolution of cosmic objects and leaves its effect in the emergence of symmetric and asymmetric structures. Thus, analyzing the symmetry criteria allows us to uncover mechanisms behind the gravity interaction and understand the underlying physical processes that contribute to the formation of large-scale structures such as galaxies. We use a segmentation process using intensity thresholding and the *k*-means clustering algorithm to analyze radio galaxy images. We employ a symmetry criterion and explore the relation between morphological symmetry in radio maps and host galaxy properties. Optical properties (stellar mass, black hole mass, optical size (R_{50}), concentration, stellar mass surface density (μ_{50}), and stellar age) and radio properties (radio flux density, radio luminosity, and radio size) are considered. We found that there is a correlation between symmetry and radio size, indicating larger radio sources have smaller symmetry indices. Therefore, size of radio sources should be considered in any investigation of symmetry. Weak correlations are also observed with other properties, such as R_{50} for FRI galaxies and stellar age. We compare the symmetry differences between FRI and FRII radio galaxies. FRII galaxies show higher symmetry in 1.4 GHz and 150 MHz maps. Investigating the influence of radio source sizes, we discovered that this result is independent of the sizes of radio sources. These findings contribute to our understanding of the morphological properties and analyses of radio galaxies.

Key words: methods: data analysis – techniques: image processing – catalogs – galaxies: nuclei – galaxies: distances and redshifts

1. Introduction

The significance of symmetry in large-scale structures and cosmic objects lies in its potential to unravel the intricate mechanisms of gravity interactions. Exploring the criteria of symmetry enables us to find the underlying mechanisms governing gravity interactions and comprehend the fundamental physical processes that contribute to the creation of large-scale structures such as clusters and galaxies. For instance, spherical symmetry in a cluster of galaxies refers to the assumption that the distribution of matter within the cluster is symmetric around a central point. This means that the cluster's properties, such as the density or temperature, are the same in all directions from the center. Spherical symmetry is particularly useful in the analysis of X-ray observations of galaxy clusters, where the emission from the hot intracluster gas is assumed to be spherically symmetric (e.g., see Sarazin 1988; Vikhlinin et al. 2006; Kravtsov & Borgani 2012). Indeed, investigating the symmetry and asymmetry of diverse phenomena and their respective definitions aids in comprehending the distinctions and resemblances among different objects (Hajdukovic 2010; Mazharimousavi et al. 2010; Kornreich et al. 1998). For instance, Mazharimousavi et al. (2010) and Kornreich et al. (1998) provide examples of symmetry definitions for distinct phenomena in symmetrical black holes and the assessment of photometric methodology for quantifying asymmetries in disk galaxies, respectively. Depending on the nature of the phenomenon, each requires a unique approach, whether through theoretical methods or observational techniques, to define symmetry.

Galaxies often exhibit different degrees of symmetry, ranging from highly symmetric spiral galaxies to more irregular and asymmetric galaxies. The level of symmetry in a galaxy can be influenced by various factors, such as the initial conditions of the galaxy's formation, interactions with neighboring galaxies, and the effects of gravitational forces (Mo et al. 2010). Symmetry in galaxies can reveal valuable information about their formation history and the physical processes at work (Sparke & Gallagher 2007). For example, spiral galaxies with well-defined arms and symmetrical structures are often associated with more orderly and stable formation processes (Stahler & Palla 2004). On the other hand, irregular and asymmetric galaxies may have experienced disruptive events such as mergers or interactions with other galaxies (Schweizer et al. 1997).

In radio passbands, symmetry also plays a crucial role in understanding the formation of radio galaxies. Symmetry in radio galaxies refers to the arrangement and distribution of their structures and features. The morphology and symmetry of the galaxies provide significant clues about their formation and evolution processes. Their symmetries and morphologies as large-scale structures can reveal insights into the underlying physical processes driving galaxy formation, such as gravitational interactions, gas dynamics, and the role of dark matter (Chibueze et al. 2021; de Gasperin et al. 2022). Moreover, focusing on nonthermal and polarized emissions of radio galaxies offers a unique perspective on active galactic nuclei (AGNs) and their evolution (Hardcastle & Croston 2020). By analyzing their various properties, such as their radio continuum spectrum, spectral index, morphology, and correlations with AGN properties at different frequencies, we can discover the intricate interplay between AGNs and their surrounding medium (Bîrzan et al. 2008). These investigations span a wide range of measurements, from very-long-baseline interferometry (VLBI) observations at parsec scales to deep observations of the larger-scale environment at megaparsecs. Also, these studies provide valuable information about the physical processes occurring around supermassive black holes (Heckman & Best 2014; Yuan & Narayan 2014).

Among a set of papers that have been established to investigate the symmetry and asymmetry in radio structures (Saikia et al. 1984; Cornwell et al. 1986; Rys 1994; Best et al. 1997; Gopal-Krishna 2000; Mantovani et al. 2003; Saikia et al. 2003; Hardcastle et al. 2005; Sarzi et al. 2006), the reader can explore how the presence of symmetry or asymmetry in the distribution of radio emission associated with a radio galaxy can indicate different formation scenarios. Symmetric radio galaxies may suggest a relatively undisturbed and stable environment during their formation, while asymmetric galaxies may imply interactions, mergers, or other dynamic processes that have disrupted their morphology (Morganti et al. 2003; Sarzi et al. 2006; Pérez-Torres & De Breuck 2005; Tadhunter 2007; Hocuk & Barthel 2010). We define symmetry criteria based on various parameters, such as proximity to the center, eccentricity, orientation, and appearance in different image quarters. Through an examination of symmetry criteria and their relation to physical parameters, we gain valuable insights into the formation and evolution of these structures.

Studies on the morphology of galaxy maps in radio passbands have led to the development of morphological classifications, which can lead to the understanding of the formation and evolution of AGN jets. The first classification scheme proposed by Fanaroff & Riley (1974) categorized radio galaxies into two groups: FRI and FRII. The FRI class is characterized by intensity peaks near the center, while the FRII class has intensity peaks near the edge. Recent studies have added compact radio sources as a third class, known as FR0 radio galaxies (Baldi et al. 2015). Research has shown correlations between radio morphology and other galaxy properties, including environmental factors. FRI radio galaxies are typically associated with dense environments and low excitation indices, while FRIIs are more prevalent in low-density environments with high-excitation AGN activity (Hill & Lilly 1991; Baum et al. 1995; Gendre et al. 2010, 2013). Subclasses of FRIs, such as bent-tailed, wide-angle-tailed (WAT), and HT radio galaxies, are useful in identifying overdensities as their jets are bent due to galaxy movement within a group or cluster (Blanton et al. 2000, 2001; Dehghan et al. 2014; O'Brien et al. 2015). The properties of radio sources with compact morphologies, such as FR0, gigahertz peaked spectrum (GPS), and compact steep-spectrum (CSS), are still being discussed as they may represent distinct populations of radio galaxies (O'Dea & Saikia 2021).

The advent of new high-resolution and sensitive radio surveys has necessitated a reevaluation of existing morphological classifications. To address this, machine-learning techniques have been employed to develop automated methods for morphological-based classification of radio galaxies (Aniyan & Thorat 2017; An et al. 2018; Lukic et al. 2018; Tang et al. 2019; Sadeghi et al. 2021). In the context of Low Frequency Array (LOFAR), novel models combining machine-learning algorithms and image analysis have been utilized, incorporating optical features of host galaxies and morphological parameters for classification purposes (Alegre et al. 2022; Barkus et al. 2022). Traditional classifications based on the location of peak intensity have been updated to account for more intricate structures observed in radio galaxy maps. Mingo et al. (2019) revealed a significant population of FRI-classified radio galaxies with core-dominant morphology transitioning from FRIIs. They also identified complex structures that do not fit within current classification definitions. Miraghaei & Best (2017) reported sources without classification, highlighting the diversity of galaxy morphologies. Given the diverse nature of galaxy morphologies observed through modern telescopes, it is essential to introduce novel automatic methods for quantifying morphologies and investigating radio maps.

In previous works, radio sources were often classified as "symmetrical" based on their compact or medium-symmetric appearance, determined manually through source brightness (Bridle et al. 1994; Readhead et al. 1996; Augusto et al. 2006). However, this classification did not automatically consider the morphological-based definition of symmetry. Bera et al. (2020) examined the symmetrical morphology of unique features like X-shaped and Z-shaped radio galaxies, considering the brightness of lobes and the angle between minor and major axes. Some studies have focused on asymmetry and its correlation with physical parameters and environmental factors in radio galaxies. The researchers in Lara et al. (2004) proposed three possible reasons for apparent asymmetry, while Laing et al. (1999) and Hocuk & Barthel (2010) discussed asymmetry in relation to luminosity and orientation, respectively. Orientation

is one of the crucial parameters that has been extensively discussed in many articles concerning radio galaxies (e.g., Podigachoski et al. 2015). Asymmetry can be observed in flux density maps, spectral index, and lobe size (Taylor et al. 1996a, 1996b; Dennett-Thorpe et al. 1999; Augusto et al. 2006). The literature also reports the detection of asymmetries in radio galaxy maps (Gopal-Krishna 2004). In this regard, the FR hybrid radio galaxies exhibit FRI characteristics on one side and FRII characteristics on the other while these asymmetries may result from orientation and line-of-sight effects, interactions between jets and the environment, or they may have fundamental explanations (Gopal-Krishna 2000; Harwood et al. 2020; Gawroński et al. 2006; Cegłowski et al. 2013). Finally, some studies have investigated asymmetry by using the fractional separation difference to assign physical properties to this measure based on the relative positions of radio intensity peaks (Banhatti 1980; Arshakian & Longair 2000; Jimenez-Gallardo et al. 2019).

The physical parameters of astrophysical objects, such as their size, temperature, density, magnetic field strength, and velocity, can have a significant impact on their radio emissions. The radio emissions from celestial objects are often associated with various physical processes, including synchrotron radiation, free–free emission, and thermal bremsstrahlung (Pacholczyk 1970). The intensity of free–free emission depends on the temperature and density of the plasma, with higher temperatures and densities leading to stronger radio emission (Condon 1992). The intensity and spectral shape of synchrotron emission depend on the strength and distribution of the magnetic field, as well as the energy distribution of the emitting particles (Longair 2011). The relationship between the physical parameters of astrophysical objects and their radio emissions has been extensively studied and documented in scientific literature (McCarthy et al. 1987; Wolter et al. 1994; Das et al. 2022).

This study builds upon previous research (Javaherian et al. 2023, hereafter, we will refer to it as paper I) that introduced a parameter known as symmetry. We provide an explanation of the methodology employed in the earlier study to address any ambiguities and enhance its clarity. The primary objective of our current investigation is to report the relationships between the symmetry as the morphological-based parameter and the other characteristics of galaxies. The layout of this article is as follows: Section 2 provides an explanation of the radio galaxy data sets and employed optical data. In Section 3, we present a review of methodology employed in paper I for the morphological analysis of radio galaxies, focusing on parameters associated with symmetry to identify their differences. To accomplish this, we offer a comprehensive workflow that encompasses preprocessing, segmentation, and parameter extraction procedures. In Section 4, we study the relationship between the physical parameters of radio galaxies (such as size, redshift, stellar mass, black hole mass, concentration, and star formation rate (SFR)) and their symmetries. Indeed, we report findings including relationships between symmetry and other properties available by the optical and radio data. Finally, Section 5 involves concluding remarks.

2. Data Analysis

2.1. Description of Radio Data Sets

The radio observations and data of radio galaxy samples have been extracted from two main radio surveys. The first data release of the LOFAR Two-meter Sky Survey (LoTSS DR1; Shimwell et al. 2017, 2019; Williams et al. 2019) and the Faint Images of the Radio Sky at Twenty-centimeters (FIRST; Becker et al. 1995) survey have been used. LoTSS is a large radio survey that maps the entire northern sky at low radio frequencies (120–168 MHz) using the LOFAR (van Haarlem et al. 2013) telescope. The LoTSS DR1 includes high-quality images and catalogs of over 300,000 radio sources detected in the survey. The FIRST radio survey, conducted at a frequency of 1.4 GHz (20-centimeter wavelength), utilizes the National Radio Astronomy Observatory's (NRAO's) Very Large Array (VLA). The FIRST survey, which detects and catalogs faint radio sources, covers the entire northern sky visible from the VLA.

The radio galaxy catalogs used in this study were selected based on the surveys presented by Miraghaei & Best (2017) and Mingo et al. (2019). Miraghaei & Best (2017) cataloged 1329 morphologically classified extended radio sources based on their 1.4 GHz radio emissions. The catalog contains radio galaxies classified as FRI, FRII, and FR hybrid, with a few sources left unclassified. In total, 608 galaxies were classified as FRI, 646 as FRII, 35 as FR hybrid, and 40 as unclassified. The radio sources were also labeled as wide-angle tailed, head-tailed (HT), diffuse, and double-double radio galaxies. Mingo et al. (2019) cataloged 5805 extended radio-loud AGNs based on the LoTSS DR1 as FRI (2965), FRII (546), and intermediate (1241). Additional labels were included, such as small, narrow-angle tailed, wide-angle tailed, and double-double radio galaxies. The intermediate sources include those that are not FRI or FRII, such as hybrid FRs, core-dominated sources (core-Ds), or fuzzy blobs.

The radio data include FITS images of a sample of 67 radio galaxies at 1.4 GHz and 150 MHz. To obtain detailed morphological information about the sources, we utilized images obtained from the FIRST cutout server at 1.4 GHz, which offered a higher resolution ($\sim 5''$) compared to the similar 1.4 GHz radio data such as NRAO VLA Sky Survey (NVSS; Condon et al. 1998) images ($\sim 45''$). This allowed us to capture more intricate details of the sources' morphologies. The noise level of these images was approximately 0.15 mJy. Additionally, we utilized the LoTSS DR1 image cutout service to extract radio images at 150 MHz. These images were mapped at two different resolutions, high ($\sim 6''$) and low

($\sim 20''$). For our study, we specifically selected high-resolution radio images as they were comparable to the resolution of FIRST, while also being more effective in detecting lower surface brightness extended sources compared to the FIRST. The LoTSS DR1 has a median sensitivity (noise level) of $S_{144\,\mathrm{MHz}} = 71\ \ \mu\mathrm{Jy.beam}^{-1}$, making it significantly more sensitive than the FIRST survey. Moreover, observing at lower frequencies offers the advantage of reduced contamination from spectral aging. The pixel sizes for FIRST and LoTSS were $1\farcs8$ and $1\farcs5$, respectively.

To construct the radio galaxy sample, a sample of 1329 FR classified radio galaxies introduced in Miraghaei & Best (2017) has been crossmatched with a sample of 5805 classified radio galaxies presented in Mingo et al. (2019). Considering the overlapping field between the two catalogs, 67 sources were selected. The crossmatch has been done using TOPCAT (Taylor 2005) to identify the closest source in the Miraghaei & Best (2017) catalog to each FR radio galaxy in the Mingo et al. (2019) catalog. A $5'$ search radius was employed to avoid overlooking any objects, resulting in the selection of 80 sources at this stage. Subsequently, a visual inspection of sources from both catalogs was conducted to verify the accuracy of the matches. In addition to eliminating incorrect matches, five hybrid sources were excluded from the final catalog. Ultimately, 67 FRI/II radio galaxies were chosen for inclusion in this analysis. The final sample consists of 34 FRI and 33 FRII radio galaxies. The FR classes of sources were taken from Miraghaei & Best (2017).

A notable difference between the classifications of Miraghaei & Best (2017) and those of Mingo et al. (2019) lies in the number of FRIIs and intermediate sources. Some FRIIs reported in Miraghaei & Best (2017) were classified as FRIs in Mingo et al. (2019), but they were all labeled as "small." Only two of them exhibited very diffused extended emissions detected by LOFAR antennas, which revealed their correct FR class. Conversely, some FRIs were classified as intermediate by Mingo et al. (2019), likely due to the high sensitivity of the survey in detecting complex structures. It is worth mentioning that our study aimed to define a parameter for evaluating the morphological properties of extended radio galaxies, regardless of their specific classifications. Therefore, the discrepancies between different classification methods did not significantly impact our analysis. For our study, we relied on the classifications presented by Miraghaei & Best (2017) while utilizing image data from both catalogs.

The radio properties used in this study include radio flux density, radio luminosity and radio size, all of which have been extracted from Miraghaei & Best (2017) in 1.4 GHz and Mingo et al. (2019) in 150 MHz. Sizes of radio sources are the total extent of the radio emission of galaxies including the jets and the core. The estimated sizes at each frequency were drawn from their parent radio catalog. We used the rest-frame radio luminosity calculated from flux densities, assuming $\alpha = 0.75$ for the spectral index (where $S_\nu \propto \nu^{-\alpha}$). For additional information regarding the utilized data sets concerning FRI and FRII galaxies and their extracted morphological properties from FIRST and LoTSS data, please refer to Tables 1 and 2 in paper I.

2.2. Description of Optical Data

Host galaxy identification and main galaxy properties are provided by the optical data. The photometric and spectroscopic data of the seventh data release (DR7; Abazajian et al. 2009) of the Sloan Digital Sky Survey (SDSS; York et al. 2000) have been exploited for this purpose. In this regard, the value-added spectroscopic catalogs of the SDSS produced by the group from the Max Planck Institute for Astrophysics and Johns Hopkins University (MPA-JHU; Brinchmann et al. 2004) include the main galaxy properties required in this work. The relevant properties are extensively discussed and used in Kauffmann papers (Kauffmann et al. 2003a, 2003b, 2003c) and the other citing papers based on the main galaxy properties of the SDSS. Total stellar mass and black hole mass, 4000 Å break strength, galaxy magnitude, half-light radius (R_{50}), concentration (C), surface mass density (μ_{50}), SFR and redshift build up the main set of galaxy optical properties. In the following, we briefly discuss them and for a complete description of these properties, we refer the readers to Mazoochi et al. (2022).

The stellar masses have been estimated via the relation

$$\text{Stellar mass} = (M/L) \times (z - \text{band luminosity}), \qquad (1)$$

where M/L is the stellar mass to light ratio of the galaxies predicted by the model. The z-band luminosity is K-corrected and dust-corrected (see Kauffmann et al. (2003b) for more details). The black hole mass (M_{BH}) is obtained from the $M-\sigma$ relation derived from $\log(M_{\mathrm{BH}}/M_\odot) = 8.13 + 4.02\log[\sigma_\star/200\ \mathrm{km\ s^{-1}}]$ (Tremaine et al. 2002). Here, σ is the velocity dispersion of the galaxies. Velocity dispersion is the result of Doppler shifting from the stellar spectra due to the stars' motion within the galaxy and has been estimated by analyzing the integrated spectrum of the whole galaxy. The velocity dispersion estimations below 70 km s^{-1}, which correspond to the $\log(M_{\mathrm{BH}}/M_\odot) \sim 6.3$, are not reliable due to the SDSS instrumental resolution for the spectra. This value falls significantly outside the range of data points in our study.

The stellar age of galaxies has been evaluated by the 4000 Å break. This feature in the spectrum of galaxies is a result of the absorption of high energy radiation from metals in the stellar atmosphere and a scarcity of hot blue stars, both of which are indicators of an old stellar population. The quantity is estimated as the ratio of the flux in the red continuum to that in the blue

continuum via the following relation (Balogh et al. 1999)

$$D_{4000} = \int_{4000}^{4100} f_\lambda \, d_\lambda \Big/ \int_{3950}^{3850} f_\lambda \, d_\lambda, \quad (2)$$

wherein f is the flux density in the wavelength of λ.

The absolute magnitude (M_r) is the K-correction of the SDSS Petrosian r-band magnitude. Correspondingly, R_{50} (or R_{90}) as a measure for the galaxy size is the radius enclosing 50 (or 90) percent of the Petrosian r-band luminosity of the galaxy (Shen et al. 2003). The surface mass density is the mean stellar mass surface density within the half-light radius, calculated via the relation $\mu_{50} = 0.5M_\star/(\pi R_{50}^2)$. Concentration index, defined as $C = R_{90}/R_{50}$, is an indicator for galaxy type. This parameter shows correlation with the optical morphology of galaxies (e.g., Strateva et al. 2001). The transition boundary between early type and late type galaxies is set at $C \sim 2.6$. The SFRs were estimated based on their relation with 4000 Å break strength (see Brinchmann et al. (2004) for more details). The redshifts of sources are spectroscopic redshifts.

3. Methodology

We have developed a new method that incorporates various preprocessing steps, including noise reduction, segmentation based on a histogram and k-means algorithm, and extraction of morphological parameters. The explanation of the proposed multi-step approach is as follows.

3.1. Segmentation Procedure

At this stage, we initially positioned the origin of each image at the center of the corresponding galaxy as seen in the visible spectrum. Subsequently, the intensities of pixels within each image were normalized relative to the maximum brightness present in that particular image. To ensure that the subsequent data analysis was conducted above the minimum noise threshold, we employed wavelet denoising techniques on each image. This denoising step helped to enhance the signal-to-noise ratio and improve the overall quality of the data for further analysis (Donoho & Johnstone 1994, Gupta et al. 2013).

In the next step, we employed the segmentation process consisting of two main steps: histogram-based intensity thresholding and the utilization of the k-means clustering segmentation algorithm. The intensity threshold is initially established based on the normalized intensities to the maximum brightness of each image. We employed a data-driven approach to identify the optimal number of bins within histograms utilized in density estimation. The optimization principle aims to minimize the expected loss function between the histogram and an unknown density function. The assumption is solely based on the independence of the samples drawn from the density (Shimazaki & Shinomoto 2007). In our study, the typical number of bins obtained for various images ranged from 8 to 13. Since we deal with brighter pixels in images, the first bins which encompass numerous pixels with lower brightness levels must be excluded from the segmentation process. Excluding the pixels in the second and third bins may have a slight impact on the results. Therefore, the starting point of the second bin is adopted as the lower limit for the intensity thresholding.

Moving on to the next step, we employed the k-means clustering algorithm for image segmentation. This algorithm is an unsupervised iterative nondeterministic method that groups features into k clusters. In our case, the features were based on the intensities and locations of pixels in the image. To begin the segmentation, pixels with intensities smaller than the lower limit of the histogram (second bin) were excluded from the procedure. The remaining pixels were then utilized as the input for the k-means clustering algorithm (Yousefzadeh et al. 2015). To better understand how this algorithm works, imagine mapping the intensities and locations of pixels to a three-dimensional feature space. The intensities would represent the third dimension in this mapping. By considering the mean distances between pixels, those with similar brightness would be grouped together in the same clusters. The criterion for intensity classification into a specific cluster is based on proximity to the mean of that particular cluster. Here, the upper limit of clusters considered in making clusters of intensities is four. Indeed, the number of segments segregated from the background of radio image can include any value between one and four.

To provide a mathematical rationale for this iterative clustering algorithm, its objective is to partition a given data set into k distinct clusters. Each cluster is represented by its centroid, which is the mean of the data points assigned to that cluster. Let $X = \{x_1, x_2, \ldots, x_n\}$ be the data set with n data points, and let $K = \{c_1, c_2, \ldots, c_k\}$ be the set of centroids representing the clusters. The algorithm follows these steps:

1. *Initialization:* Randomly initialize the centroids c_1, $c_2, \ldots, c_k$.
2. *Assignment:* Assign each data point x_i to the nearest centroid c_j based on the Euclidean distance $d(x_i, c_j)$:

$$\min_j d(x_i, c_j) = \min_j \sqrt{\sum_{l=1}^{\Gamma} (x_{il} - c_{jl})^2},$$

   where Γ is the dimensionality of the data points.
3. *Update:* Update the centroids c_j by calculating the mean of the data points assigned to each cluster:

$$c_j = \frac{1}{|C_j|} \sum_{x_i \in C_j} x_i,$$

   where C_j is the set of data points assigned to cluster j.
4. *Termination:* Repeat steps 2 and 3 until convergence criteria are met. Convergence is typically achieved when the centroids no longer change significantly or after a fixed number of iterations.

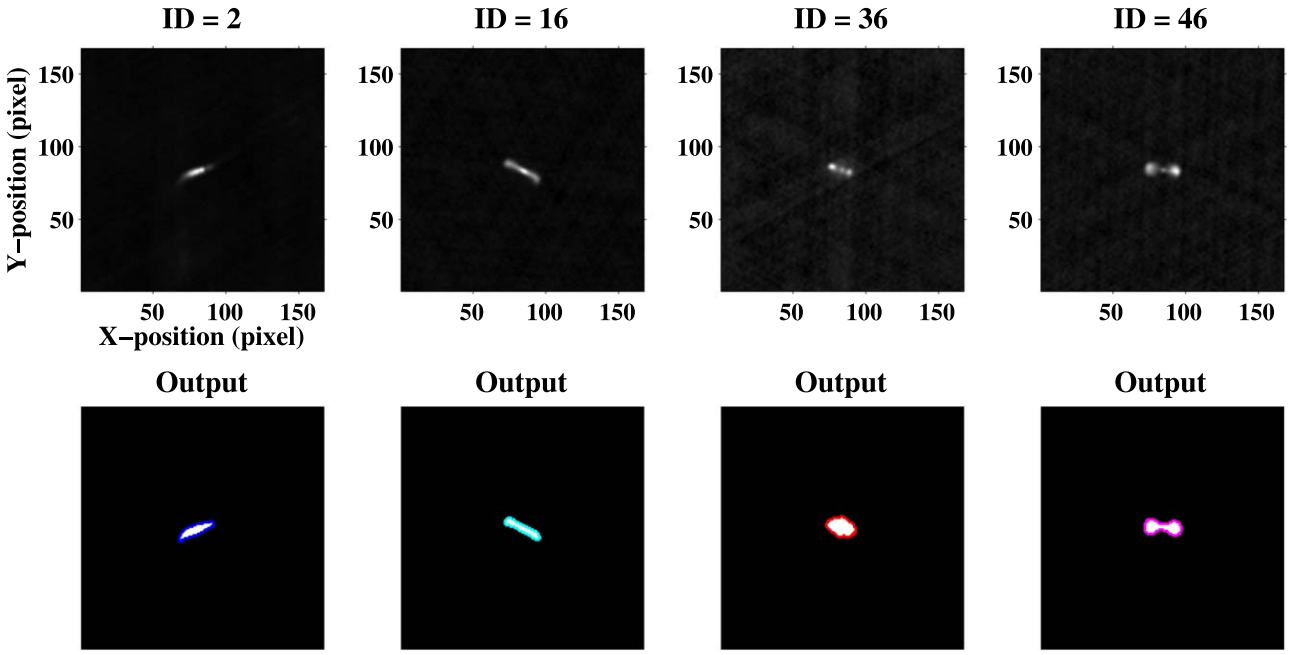

Figure 1. The first row shows the original images of FIRST data with IDs 2 and 16 belonging to the type 1 radio galaxies, and IDs 36 and 46 belonging to the type 2 radio galaxies. The second row demonstrates the outputs of the segmentation process. The borders of segments are displayed with different colors.

The k-means algorithm aims to minimize the within-cluster sum of squares, also known as the inertia, defined as

$$\sum_{j=1}^{k} \sum_{x_i \in C_j} \|x_i - c_j\|^2,$$

where $\|x_i - c_j\|$ denotes the Euclidean distance between data point x_i and centroid c_j. The outputs of procedures for FIRST and LoTSS galaxies are demonstrated in Figures 1 and 2, respectively. It should be mentioned that the cutout images in both FIRST and LoTSS data sets are the same size in radians, but differ in the number of pixels due to varying data resolutions. For specific details of the cutout images (such as pixels and radians) in the two data sets, the reader can refer to Tables 1 and 2 in paper I.

3.2. Intensity-weighted Centroid, Orientation, and Eccentricity

Once the objects have been separated, the region(s) with their initial intensities are preserved. To determine the intensity-weighted centroid (IWC), eccentricity, and orientation of each region, we employed the central moments of the image (Noori et al. 2019, Tajik et al. 2023). The central moments μ_{pq} of an image $I(x, y)$ are calculated using the following formula

$$\mu_{pq} = \sum_x \sum_y (x - X_{\rm IWC})^p (y - Y_{\rm IWC})^q I(x, y). \quad (3)$$

The coordinates of the IWC, denoted as $X_{IWC} = \frac{m_{10}}{m_{00}}$ and $Y_{\rm IWC} = \frac{m_{01}}{m_{00}}$, can be obtained using the following method

$$m_{pq} = \sum_x \sum_y x^p y^q I(x, y). \quad (4)$$

So, for a binary image, the zero-order moment m_{00} represents the area A of the segmented region labeled one. By determining the centroid, we can obtain the Cartesian coordinates of a quarter of the target. The orientation ϕ of the object relative to the positive x-axis can be expressed as

$$\phi = \frac{1}{2} \arctan\left(\frac{2\mu_{11}}{\mu_{20} - \mu_{02}}\right). \quad (5)$$

By utilizing the orientation and fitting the bounding box of the object, we can calculate the major axis (a) and subsequently the minor axis (b) of its shape. Therefore, the eccentricity (ε) can be determined through the following equation

$$\varepsilon = \sqrt{1 - \frac{b^2}{a^2}}. \quad (6)$$

Figure 3 illustrates the ellipses with different eccentricities aligned along the positive x-axis ($\phi = 0$).

3.3. Symmetry Definition

The definition we propose for symmetry is not influenced by the spatial orientation of the galaxy in the image. The only requirements are that the center of the captured image aligns

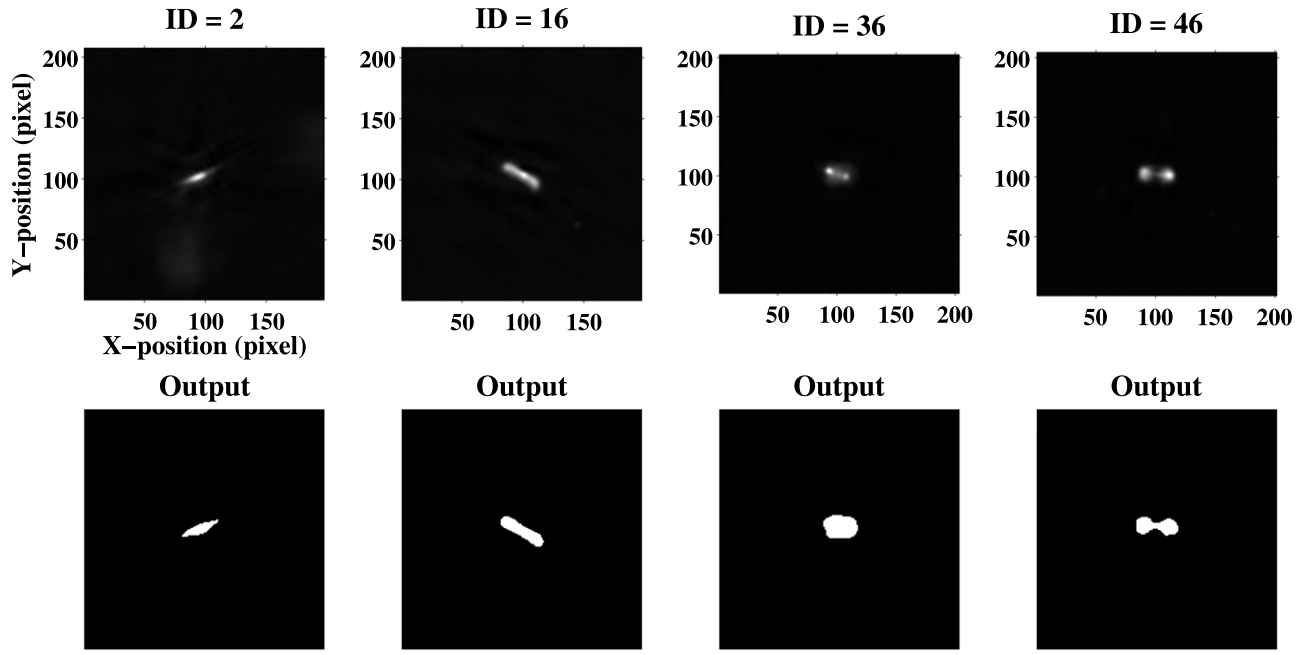

Figure 2. The first row shows the original images of LoTSS data with IDs 2 and 16 belonging to the type 1 radio galaxies, and IDs 36 and 46 belonging to the type 2 radio galaxies. The second row demonstrates the outputs of the segmentation process.

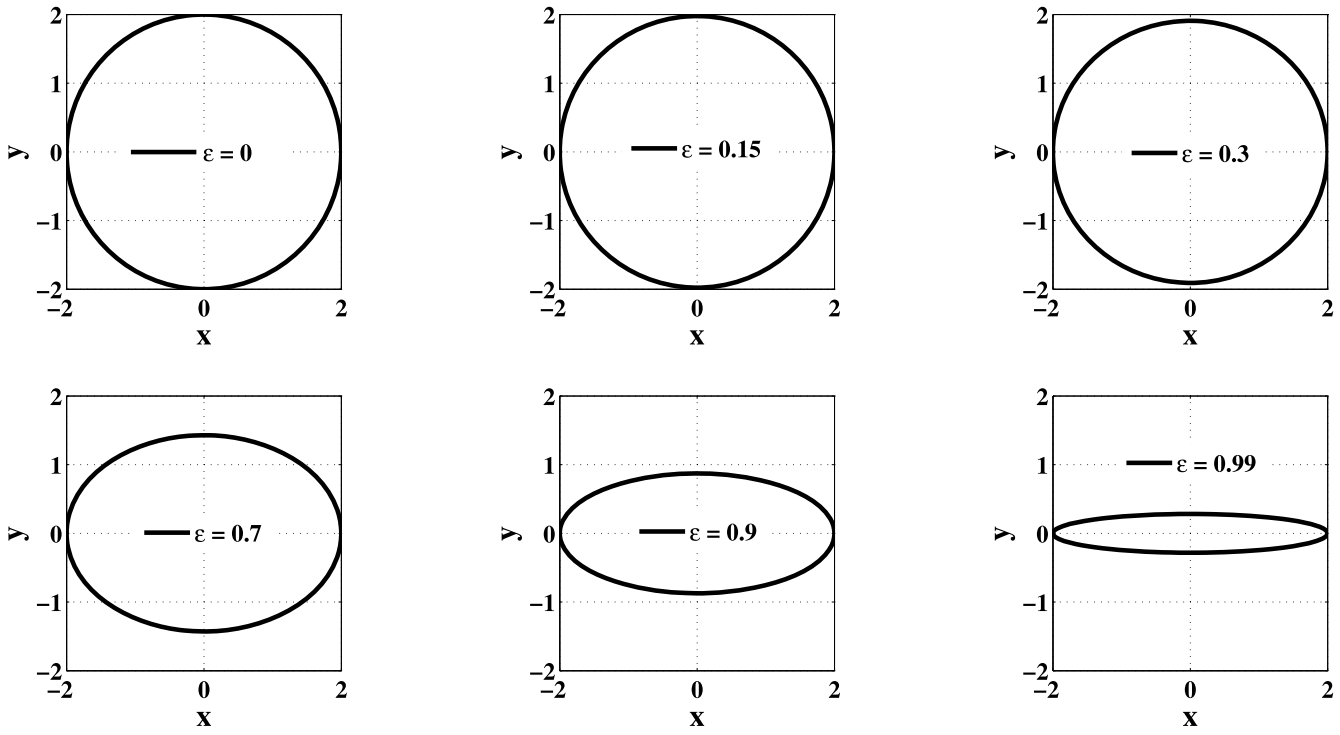

Figure 3. The plot displays six ellipses, each with an orientation of $\phi = 0$ and a distinct eccentricity.

with the optical center of the galaxy, and that all images have an equal area (5′ in two catalogs). Therefore, to establish symmetry parameters related to the center of galaxies in the optical band, we need to consider symmetry criteria based on the morphological characteristics of the extracted regions in galaxy maps. The code takes the size of the image as input to determine a quarter of the segmented region and the distance between the intensity centroid of the region and the center of the image (i.e., the center of the galaxy in the optical band).

For an image with a single segmented region, we calculate the symmetry of the region, denoted as $\mathcal{S}$, by multiplying two symmetries: one related to the proximity of the region centroid to the center of the image ($\mathcal{S}_{\rm proximity}$), and the other related to the eccentricity of the region ($\mathcal{S}_{\rm eccentricity}$). For example, for an elongated object with $\varepsilon = 0.9$ (see Figure 3) $\mathcal{S}_{\rm eccentricity}$ is obtained as $|\frac{1-0.9}{1}| = 0.1$. So, for a segmented region with $\varepsilon = 1$ (see Figure 3), we obtain $|\frac{1-1}{1}| = 0$ for $\mathcal{S}_{\rm eccentricity}$. When dealing with an image containing multiple segmented regions, in addition to the previous symmetries (with a slight difference in the definition of the symmetry of proximity), we also define two symmetries associated with the quarters ($\mathcal{S}_{\rm quarter}$) and orientations ($\mathcal{S}_{\rm orientation}$) of the segmented regions. The range of all symmetries is [0, 1]. A symmetry value of one indicates the highest level of symmetry for the region, while a value of zero represents the lowest level of symmetry. The multiplication of these symmetries results in a final symmetry value specific to the case of interest, which also falls within the range [0, 1]. We describe in detail four different cases depending on the number of segregated regions observed in each map:

Case 1: This case corresponds to radio maps with only one segmented region. It involves analyzing a segmented region in an image that is either close to or far from the center (as shown by the green circles in Shape I of Figure 4). The first symmetry parameter is defined based on the proximity of the IWC of a region to the center of the image (i.e., the center of the galaxy in the optical band). A proximity measure, denoted as $\mathcal{S}_{\rm proximity}$, is assigned a value of one if the centroid of the region is positioned at the center of the image. A value of zero is assigned when the centroid is positioned exactly at the outer edge of the circle enclosed by the square, which represents the image data. This indicates that the centroid coincides with the boundary of the circle within the square region. For instance, for an image with 201×201 pixels, we consider a circle with a radius of 100 pixels where the center of the circle is located at the 101st pixel. If the IWC of a segmented region falls on the circumference of the circle enclosed by the square (i.e., image data), $\mathcal{S}_{\rm proximity}$ is calculated as $|\frac{101-101}{101}| = 0$. Please refer to Figure 4, Shape I, Regions 2 and 3.

To account for the fact that circle-like shapes exhibit more symmetry than elongated shapes, we introduce a second measure of symmetry related to the eccentricity parameter. If the eccentricity of a shape returns a value of zero (indicating a circle), we assign a symmetry measure, denoted as $\mathcal{S}_{\rm eccentricity}$, a value of one. Conversely, shapes with eccentricities of 1 (representing a line) are assigned a value of zero for $\mathcal{S}_{\rm eccentricity}$. Therefore, the multiplication of these parameters, $\mathcal{S}_{\rm proximity} \times \mathcal{S}_{\rm eccentricity}$, yields a symmetry criterion, denoted as $\mathcal{S}$, ranging from zero (completely asymmetric) to one (perfectly symmetric).

For instance, let us consider the case of a segmented radio galaxy with ID number 43 (refer to Table 2 in paper I) in the LoTSS data. The distance of its IWC to the center of the image is one pixel (1.″5), and the image size is 202^2 pixels. The distance from the center of the image to the end of the area of interest is 101 pixels (151.″5). Therefore, $\mathcal{S}_{\rm proximity}$ can be calculated as 0.99 (i.e., $|\frac{101-1}{101}|$ or $|\frac{151.5-1.5}{151.5}|$). As we selected all image tiles in both catalogs with an area of 5′ and the specified criterion is formulated to yield symmetry values within the range of 0–1, the results are not affected by the image size (i.e., the unit of arcsec (arcmin) is omitted from the numerator and denominator of the fraction of defined formula). Additionally, the eccentricity of the object is 0.80, resulting in a value of 0.20 (i.e., $\frac{1-0.80}{1}$) for $\mathcal{S}_{\rm eccentricity}$. Consequently, the multiplication of these parameters yields a symmetry criterion of $\mathcal{S} = 0.20$.

Case 2: This case involves radio maps with two segmented regions. The symmetry for the two regions is determined by two parameters: quarters and proximity. To define symmetry in terms of quarters, we consider the IWCs of the regions. We use the notations q' and q'' to represent the quarters in which the IWCs of the first and second segments appear, respectively. The centroids must be in quarters where the absolute difference between q' and q'' is 2. If the centroids are in quarters 1 and 3 or quarters 2 and 4, then the symmetry parameter $\mathcal{S}_{\rm quarter}$ is 1; otherwise, it is 0.

The proximity of the centroids to the center of the image is another parameter. We update the definition of $\mathcal{S}_{\rm proximity}$ to illustrate the symmetry in two segmented sources. When the centroids are equidistant from the center of the image, $\mathcal{S}_{\rm proximity}$ is 1. If they are farthest apart, with one at the point closest to the center and the other at the farthest point from the center (on a radius of the circle), then $\mathcal{S}_{\rm proximity}$ is 0. To compute $\mathcal{S}_{\rm proximity}$, we use the formula $\frac{\text{radius of the circle (half} - \text{image size)} - |\, Dq' - D_{q''}\,|}{\text{radius of the circle (half} - \text{image size)}}$, where $D_{q'}$ and $D_{q''}$ are the distances of the centroids from the center of the image in quarters q' and q'', respectively. Thus, the defined criterion is structured to produce symmetry values within the range of 0–1. As we previously mentioned, since we selected images with the same size of 5′, the results are not affected by the image size.

The similarity of regions in terms of eccentricity and orientation is captured by two additional parameters: $\mathcal{S}_{\rm eccentricity}$ and $\mathcal{S}_{\rm orientation}$. For $\mathcal{S}_{\rm eccentricity}$, if the regions in two quarters have the same eccentricities, $\mathcal{S}_{\rm eccentricity}$ is 1. If the

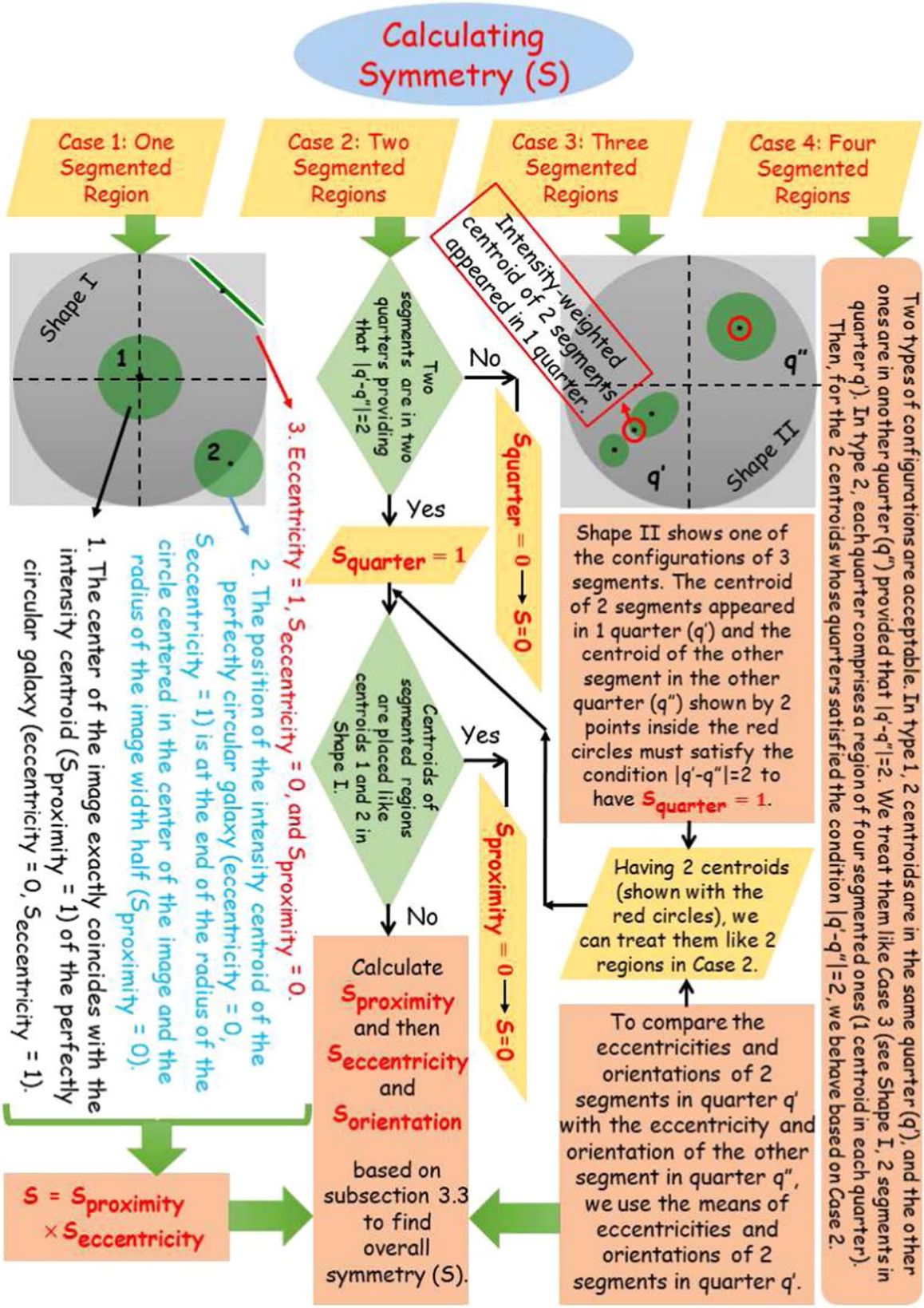

Figure 4. Flowchart of presented work (see text for more details). Artificial images including green objects (mimicking segments of radio galaxies) in different quarters.

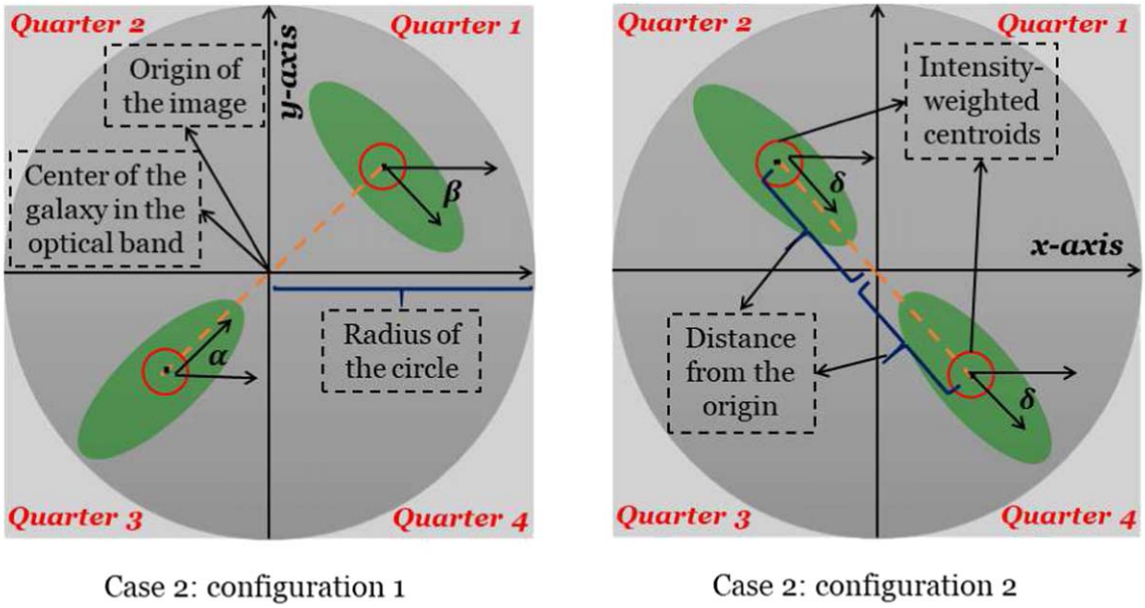

Figure 5. Artificial images mimicking radio galaxy images include green objects representing segments of radio galaxies placed in various quadrants. We see two possible configurations of two segments, as described in Case 2, with the condition $\mathcal{S}_{\rm quarter} = 1$. The distances of the centroids from the origin are represented by orange dashed lines, which have equal lengths. Consequently, the definition of $\mathcal{S}_{\rm proximity}$ assigns a value of 1 to both configurations. The eccentricities of all segments in both configurations are 0.93. In both panels, since the eccentricity values are the same, $\mathcal{S}_{\rm eccentricity}$ is calculated as $\frac{1-|\,0.93-0.93\,|}{1} = 1$. In the left panel, the segment in quarter 1 has a negative angle relative to the positive x-axis, $\beta = -45°$, while the segment in quarter 3 has an angle of $\alpha = 45°$ relative to the positive x-axis. Therefore, $\mathcal{S}_{\rm orientation}$ is obtained as $\frac{90-|\,-45-45\,|}{90} = 0$. By multiplying $\mathcal{S}_{\rm quarter}$, $\mathcal{S}_{\rm proximity}$, $\mathcal{S}_{\rm eccentricity}$, and $\mathcal{S}_{\rm orientation}$, the resulting symmetry value is 0. On the other hand, in the right panel, the segments in quarters 2 and 4 have a negative angle relative to the positive x-axis, $\delta = -45°$, resulting in $\mathcal{S}_{\rm orientation} = 1$. Thus, the symmetry value is 1 for this configuration when all four defined parameters in Case 2 are multiplied together.

difference between eccentricities is maximum (1–0 = 1) for the two regions, then $\mathcal{S}_{\rm eccentricity}$ is 0. The formula used to compute $\mathcal{S}_{\rm eccentricity}$ is $\frac{1-|\,\varepsilon_{q'}-\varepsilon_{q''}\,|}{1}$, where $\varepsilon_{q'}$ and $\varepsilon_{q''}$ are the eccentricities of regions in quarters q' and q'', respectively. For $\mathcal{S}_{\rm orientation}$, if two regions have the same angles of orientation, $\mathcal{S}_{\rm orientation}$ is 1. If the bending angle between two regions is 90°, then $\mathcal{S}_{\rm orientation}$ is 0. The formula used to compute $\mathcal{S}_{\rm orientation}$ is $\frac{90-|\,\phi_{q'}-\phi_{q''}\,|}{90}$, where $\phi_{q'}$ and $\phi_{q''}$ are the orientations of regions in quarters q' and q'', respectively.

The symmetry criterion for two regions is given by the multiplication of all these parameters: $\mathcal{S} = \mathcal{S}_{\rm quarter} \times \mathcal{S}_{\rm proximity} \times \mathcal{S}_{\rm eccentricity} \times \mathcal{S}_{\rm orientation}$. For example,we analyze the symmetry parameters for a radio galaxy with ID number 1 in FIRST data. Since $|2-4| = 2$, $\mathcal{S}_{\rm quarter} = 1$. Using an image size of 167^2 pixels, we compute $\mathcal{S}_{\rm proximity}$ as $\frac{(167/2)-|\,12.10-21.32\,|}{(167/2)}$, $\mathcal{S}_{\rm eccentricity}$ as $\frac{1-|\,0.98-0.92\,|}{1}$, and $\mathcal{S}_{\rm orientation}$ as $\frac{90-|\,-37.91-(-42.64)\,|}{90}$. The multiplication of these parameters gives $\mathcal{S} = 0.80$. We present two potential configurations of artificial segments that mimic galaxies (objects with green color) in Figure 5. We consider two configurations satisfying the condition $|q' - q''| = 2$ with $\mathcal{S}_{\rm proximity} \times \mathcal{S}_{\rm eccentricity} = 1$. The reader can refer to the caption of Figure 5 for detailed explanations of the illustrations and the symmetry computations for this typical example.

Case 3: This scenario pertains to radio maps that feature three segmented regions. In this case, the only accepted system of positioning regions is as follows: two regions in the same quarter, and the third region in another quarter, provided that $|q' - q''| = 2$ (refer to Shape II in Figure 4 for one of the acceptable configurations). To proceed, we first determine the centroid, as well as the mean eccentricities and orientations, of the two segments in one quarter. We follow the same approach as in the previous case. Based on this, we can determine whether $\mathcal{S}_{\rm quarter} = 1$;, otherwise $\mathcal{S}_{\rm quarter} = 0$. An example that satisfies this criterion is the radio galaxy with ID number 15 in the LoTSS data (see Table 1 in paper I), which exhibits three segregated regions within two quarters: one region in the first quarter and two regions in the third quarter. Since $|1-3| = 2$, we have $\mathcal{S}_{\rm quarter} = 1$. Among the 67 galaxies in two catalogs, two galaxies in the FIRST catalog and three galaxies in the LoTSS catalog have three segments. Out of the two galaxies (with ID numbers 44 and 61) from the FIRST catalog, one (with ID number 61) met our defined symmetry condition regarding quarters, while the other (representing 1/67 of the entire FIRST data set) takes a symmetry value of zero. Among the three galaxies from the LoTSS catalog (with ID numbers

Table 1
Obtained Values for Symmetries ($\mathcal{S}$) of Radio Galaxies Observed in FIRST (F) and LoTSS (L) Data

Type 1 Radio Galaxies						Type 2 Radio Galaxies					
ID	$\mathcal{S}_F$	$\mathcal{S}_L$	ID	$\mathcal{S}_F$	$\mathcal{S}_L$	ID	$\mathcal{S}_F$	$\mathcal{S}_L$	ID	$\mathcal{S}_F$	$\mathcal{S}_L$
1	0.80	0.83	2	0.03	0.04	35	0.11	0.22	36	0.21	0.29
3	0.37	0.07	4	0.07	0.06	37	0.39	0.10	38	0.09	0.10
5	0.05	0.07	6	0.96	0.03	39	0.82	0.63	40	0.12	0.16
7	0.03	0.02	8	0.16	0.18	41	0.19	0.27	42	0.53	0.31
9	0.13	0.14	10	0.04	0.01	43	0.13	0.20	44	0	0.39
11	0.01	0.02	12	0.04	0.11	45	0.10	0.14	46	0.05	0.07
13	0.03	0.02	14	0	0	47	0.03	0.06	48	0.46	0.03
15	0	0.67	16	0.02	0.04	49	0.17	0.18	50	0.05	0.11
17	0.24	0	18	0.09	0	51	0.12	0.11	52	0.15	0.25
19	0.05	0.12	20	0.13	0.13	53	0.88	0.70	54	0.11	0.14
21	0.24	0	22	0.05	0.04	55	0.17	0.20	56	0.07	0.13
23	0.17	0.03	24	0	0	57	0.15	0	58	0.14	0.15
25	0.03	0.05	26	0.47	0.02	59	0.03	0.08	60	0.03	0.06
27	0	0	28	0.36	0.07	61	0.39	0.07	62	0.29	0.13
29	0.12	0.04	30	0.05	0.05	63	0.02	0.05	64	0.15	0.24
31	0.05	0.08	32	0.10	0.16	65	0.77	0.01	66	0.04	0.07
33	0.66	0.58	34	0.09	0.13	67	0.04	0.05	…	…	…

15, 21, and 24), one (with ID number 15) satisfies the defined symmetry criterion, while the remaining two (equivalent to $2/67$ of the entire LoTSS data set) take a symmetry value of zero. According to our symmetry definition, if the defined condition is not met, no symmetry is observed relative to the optical center.

In the subsequent step, we calculate the centroid of the two weighted centroids of the regions in the same quarter (represented by the red circles in Shape II of Figure 4). Subsequently, we compare the distances between the two centroids and the center of the image in quarters 1 and 3. We then proceed with the same method as the previous case to determine $\mathcal{S}_{\text{proximity}}$. To calculate $\mathcal{S}_{\text{eccentricity}}$ and $\mathcal{S}_{\text{orientation}}$, we use the means of the eccentricities and orientations of the regions in the same quarter. These values are then compared with the eccentricities and orientations of the region in the other quarter, respectively. Consequently, we can define a symmetric criterion for the positioning of three regions in a radio map using the last relation provided in Case 2 for the two regions.

Case 4: This scenario corresponds to radio maps featuring four segmented regions. For this case, there are three configurations, all meeting the condition of $\mathcal{S}_{\text{quarter}} = 1$. Among the various types of positioning for four regions in radio maps, we can establish symmetric criteria for only two systems of positioning.

In the first type of positioning, each quarter contains a region composed of four segmented parts. For the two regions whose quarters satisfy the condition $|q' - q''| = 2$, we apply the principles outlined in Case 2. Consequently, the requirements of symmetry must solely be fulfilled by the two regions that face each other with respect to the optical center. In the second type of positioning, two regions are situated in the same quarter, while the other two regions are located in another quarter, provided that $|q' - q''| = 2$. Similar to the previous case involving two regions in a quarter, we can perform all the necessary tasks for the two regions in their respective quarters. This involves determining the centroids and calculating the means of eccentricities and orientations for the regions in each quarter. Then, we can compare all the obtained parameters, similar to Case 2, to establish the symmetric criterion. It is worth mentioning that among the 67 galaxies in two catalogs, one galaxy (i.e., $1/67$ of the entire data set) in the FIRST catalog (with ID number 15) and one galaxy (i.e., $1/67$ of the entire data set) in the LoTSS catalog (with ID number 57) have four segments. Their symmetry value is zero because they do not have the defined quarter-based symmetry.

We computed symmetry for FRI and FRII galaxies using FIRST ($\mathcal{S}_F$) and LoTSS ($\mathcal{S}_L$) data sets (Table 1). The mean symmetries for images with one segmented region are 0.11 for both FIRST and LoTSS data sets. For images with two segmented regions, the mean symmetries are 0.39 and 0.32 for FIRST and LoTSS sets, respectively. Images with three or four regions have lower mean symmetries. As is seen in Table 1, the highest symmetry value belongs to a type 2 galaxy (ID = 53) with two segmented regions, with symmetries of 0.88 in FIRST data and 0.70 in LoTSS data.

4. Results and Discussions

4.1. Symmetry and Main Properties of Galaxy

In this section, we used the parameter defined and calculated to quantify morphological symmetry in radio maps of galaxies

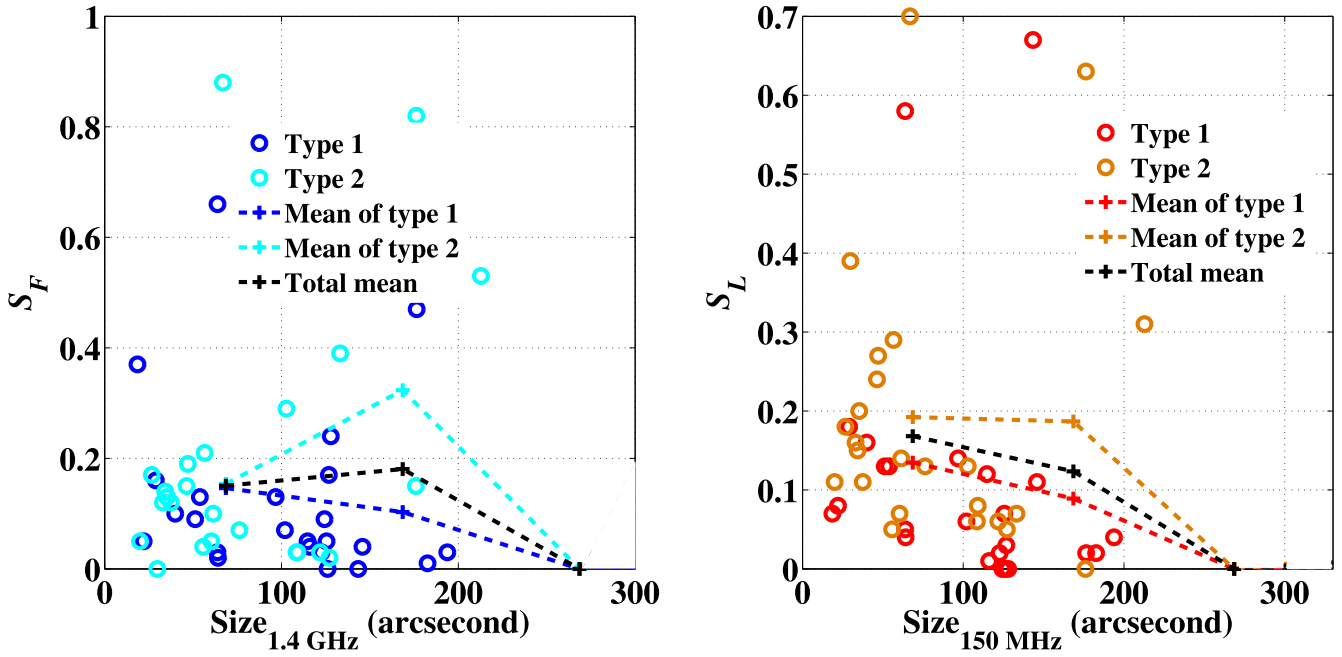

Figure 6. The relationships between the symmetry of galaxies and their sizes (arcsecond) for mean values (shown by a +) of each bin (25, 125, etc.) for the FIRST and LoTSS data are demonstrated in the left and right scatter plots, respectively. The blue circles and cyan circles belong to type 1 and type 2 galaxies, respectively, in the FIRST data. The red circles and orange circles belong to type 1 and type 2 galaxies, respectively, in the LoTSS data. (Hereafter, we omit the legends of panels in all figures because they are the same.)

and investigate any relation between symmetry and properties of the host galaxy. There are two sets of properties: (1) The radio properties which include radio size, radio flux density, and radio luminosity; (2) The optical properties which include stellar mass, black hole mass, R_{50}, concentration, μ_{50}, stellar age, and SFR.

We examine the total sample of radio galaxies, and the FRI and the FRII subsamples to find if there are any type dependence behavior related to the symmetry parameter. In the first step, we plot the two-dimensional maps of the symmetry versus other properties of the galaxies in Figures 6–17. Figures 6–7 display scatter plots depicting the relationship between symmetry and sizes of radio sources in various passbands. Across all right-hand sides of the scatter plots, there is a noticeable decrease in the total means of symmetries with increasing sizes. In both panels of Figure 8, a downward trend in total means of symmetries is observed as flux densities increase. The scatter plots in Figure 9 depicting symmetries of galaxies and their luminosities illustrate that the total mean of symmetries remains approximately constant from low to high luminosities. Analyzing the scatter plots of symmetries and redshifts in Figure 10 reveals that the total mean symmetries of higher redshifts are relatively less than those in lower redshifts.

The scatter plots of symmetries versus stellar masses in Figure 11 reach a maximum value in total means of symmetries near $10^{11}\ M_{\odot}$. Subsequently, the total means of symmetries gradually decrease to $10^{11.5}\ M_{\odot}$ in both the FIRST and LoTSS data sets. However, the trend of the total mean of the left-side scatter increases, contrary to the right-side scatter. Figure 12 displays scatter plots of symmetries versus black hole masses. The total means of symmetries demonstrate fluctuations around 0.2 and 0.15 $\log(M_{\rm BH}/M_{\odot})$ for FIRST (left panel) and LoTSS (right panel), respectively. The scatter plots of symmetries versus R_{50} which is an optical size for the host galaxies of radio sources are represented in Figure 13. The left scatter plot of Figure 13 shows an almost downward trend in mean symmetry of FIRST data from lower to higher values of R_{50}; while the mean symmetry of LoTSS data is approximately constant throughout the x-axis in the right panel of Figure 13 belonging to LoTSS data. The mean symmetries reach their minimum values around the concentration value of 3.2 in both scatter plots of Figure 14. In both scatter plots of Figure 15, we observe an increasing trend for mean symmetries after the value of $10^{8.9}\ M_{\odot}\ {\rm kpc}^{-2}$ for $\mu_{\rm star}$. Looking at the scatter plots of symmetries versus stellar age, we find that there is a maximum symmetry around the stellar age of 1.75 for both panels of Figure 16. Subsequently, the trends of mean symmetries decrease for both plots around the stellar ages of 2.05 and 2.15 for FIRST and LoTSS data sets, respectively. Figure 17 illustrates the scatter plots of symmetries versus SFR, showing that the mean symmetry gently increases with the rising SFR in LoTSS data.

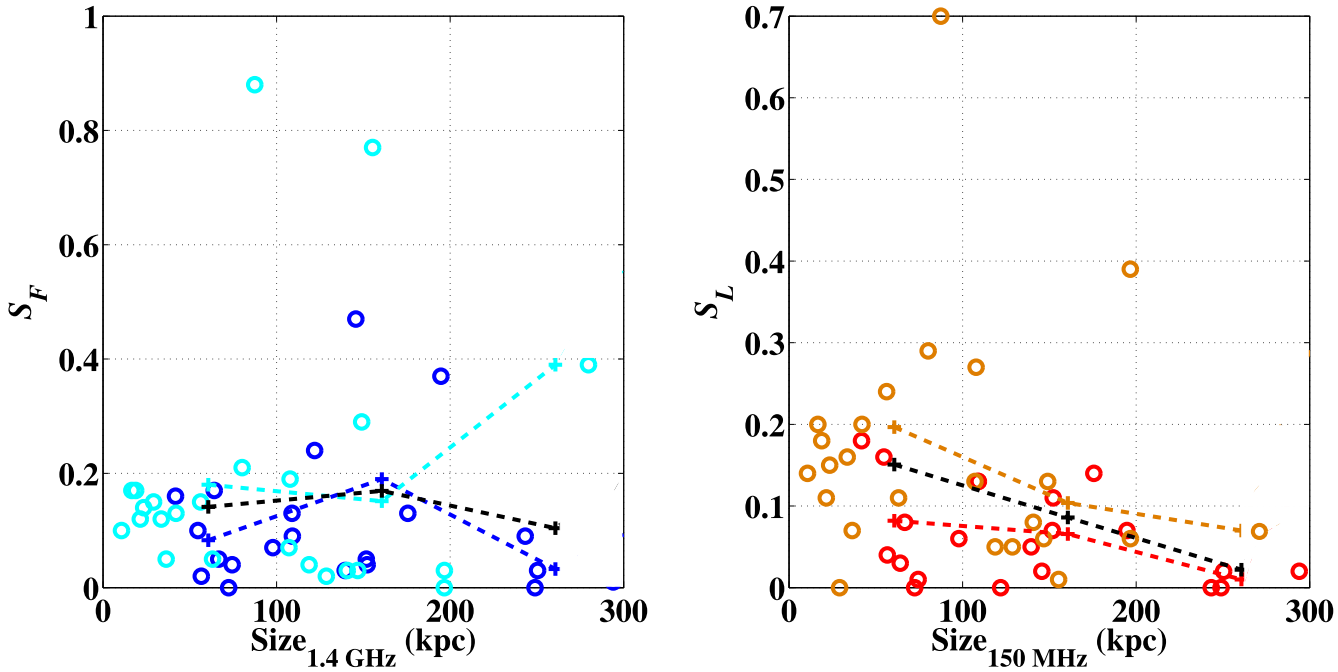

Figure 7. The relationships between the symmetry of galaxies and their sizes (kpc) for mean values (shown by a +) of each bin (25, 125, etc.) for the FIRST and LoTSS data are demonstrated in the left and right scatter plots, respectively. The symbols are the same as those in Figure 6.

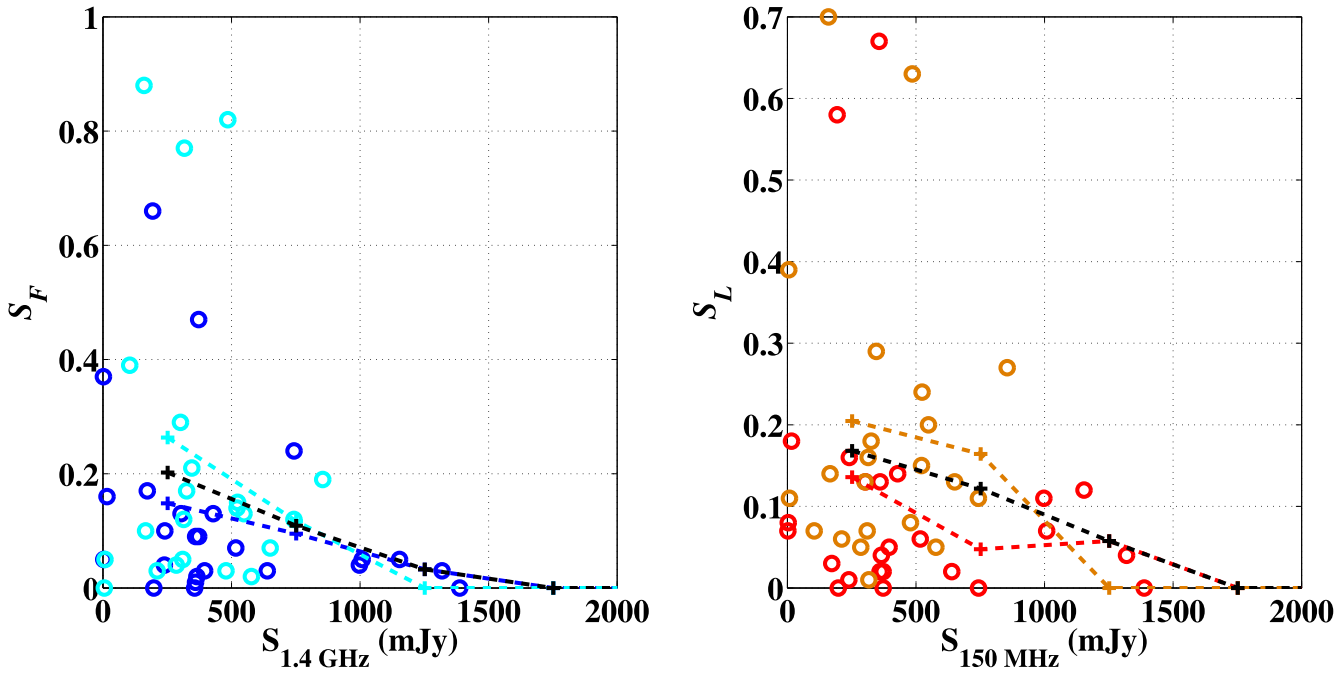

Figure 8. The relationships between the symmetry of galaxies and their flux density for mean values (shown by a +) of each bin (0, 500, etc.) for the FIRST and LoTSS data are demonstrated in the left and right scatter plots, respectively. The symbols are the same as those in Figure 6.

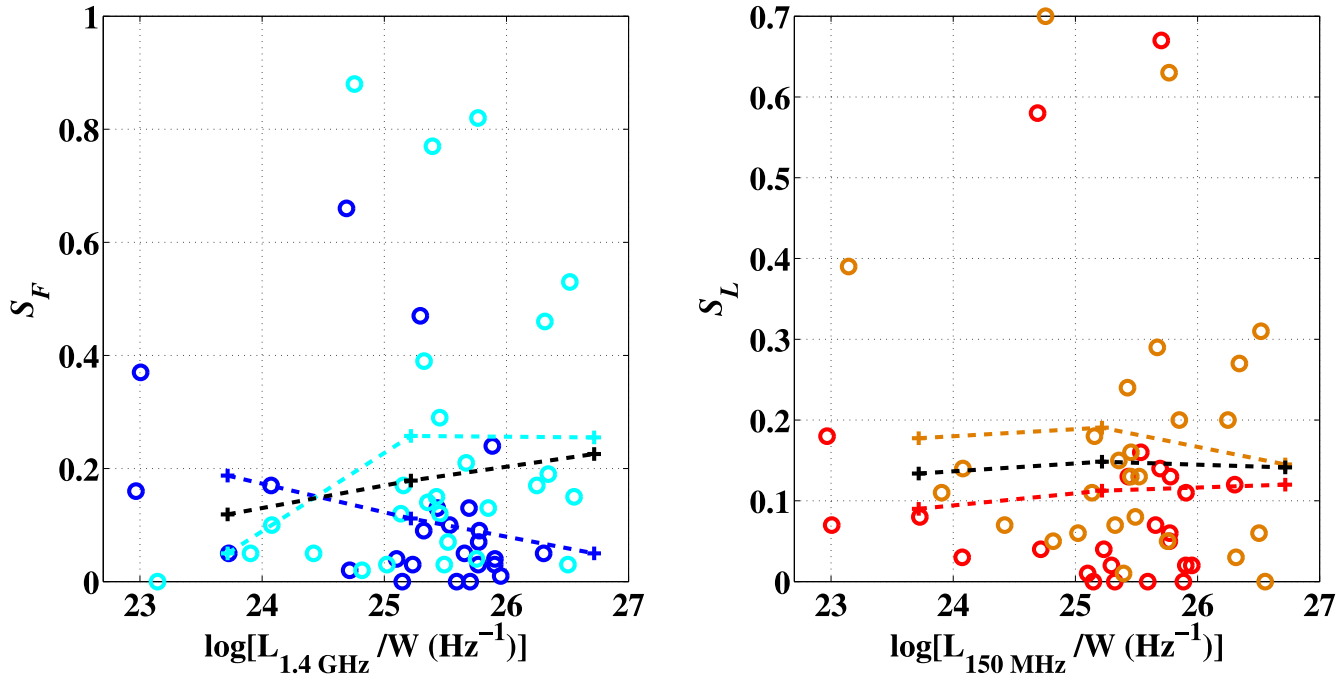

Figure 9. The relationships between the symmetry of galaxies and their luminosities for mean values (shown by a +) of each bin (22.75, 24.25, etc.) for the FIRST and LoTSS data are demonstrated in the left and right scatter plots, respectively. The symbols are the same as those in Figure 6.

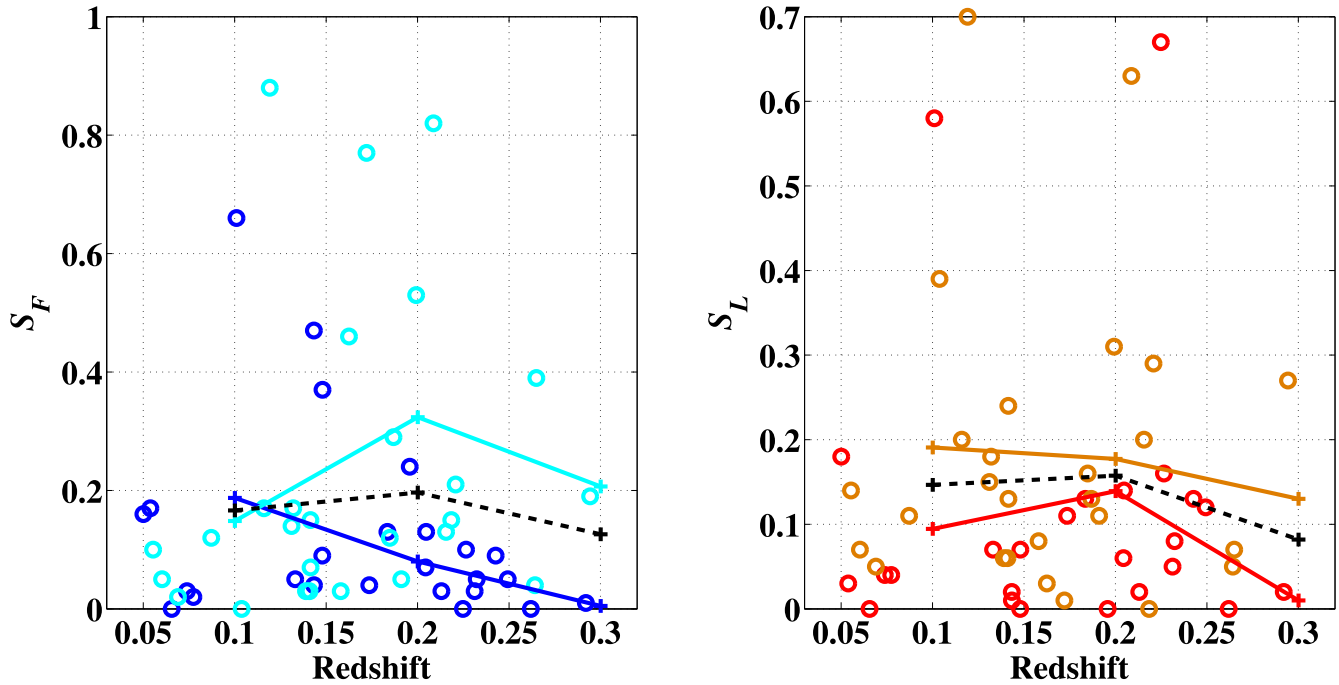

Figure 10. The relationships between the symmetry of galaxies and their redshift for mean values (shown by a +) of each bin (0.05, 0.15, etc.) for the FIRST and LoTSS data are demonstrated in the left and right scatter plots, respectively. The symbols are the same as those in Figure 6.

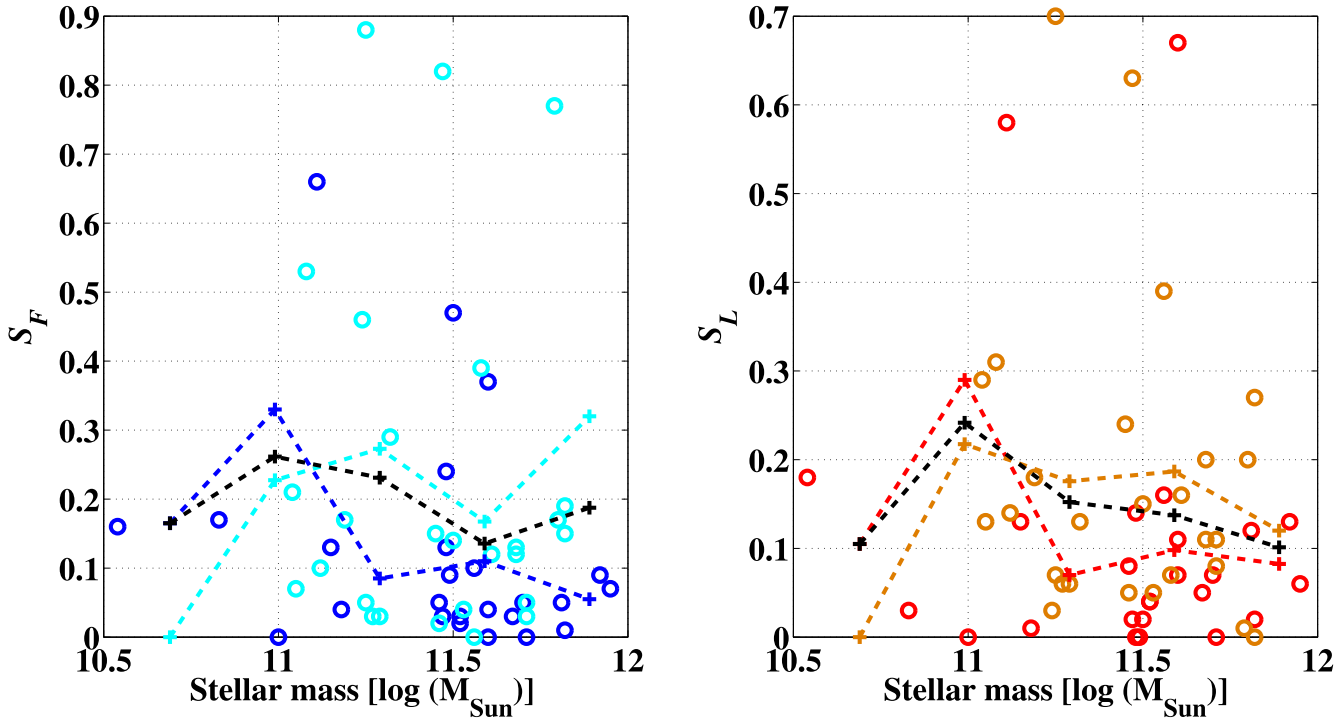

Figure 11. The relationships between the symmetry of galaxies and stellar masses for mean values (shown by a +) of each bin (10.5, 10.8, 11.1, etc.) for the FIRST and LoTSS data are demonstrated in the left and right scatter plots, respectively. The symbols are the same as those in Figure 6.

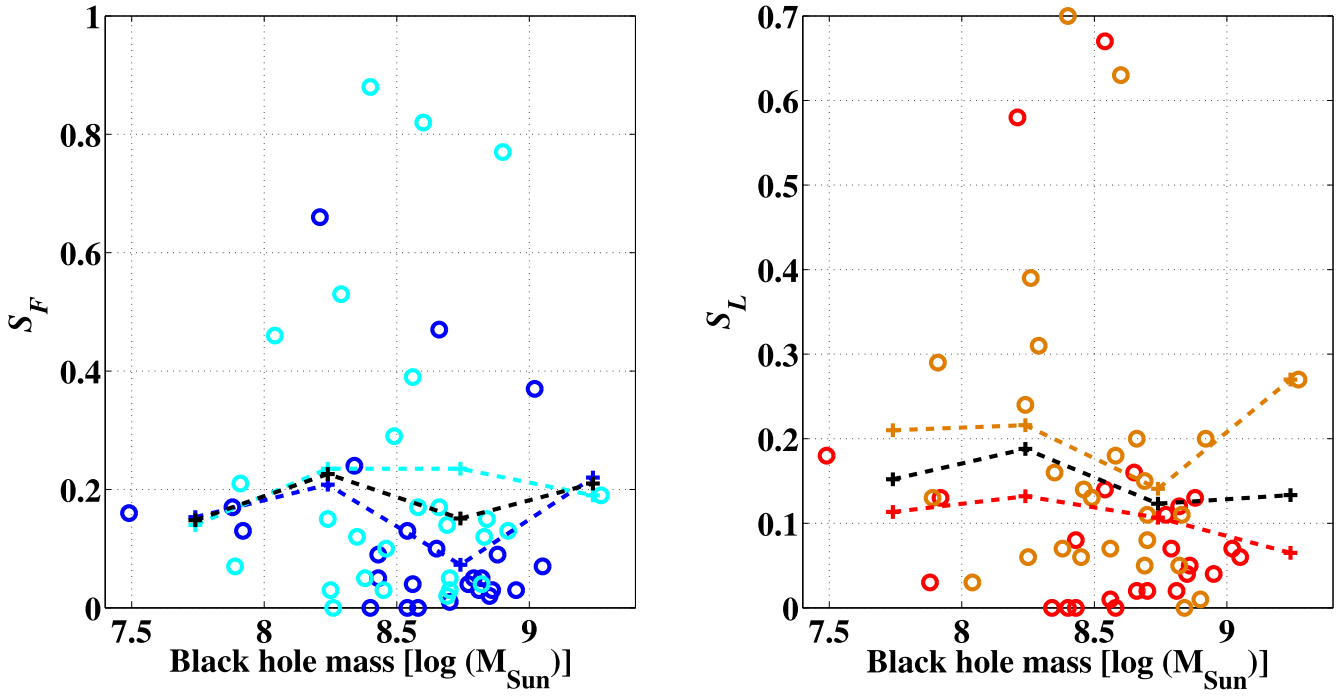

Figure 12. The relationships between the symmetry of galaxies and black hole masses for mean values (shown by a +) of each bin (7.5, 8, etc.) for the FIRST and LoTSS data are demonstrated in the left and right scatter plots, respectively. The symbols are the same as those in Figure 6.

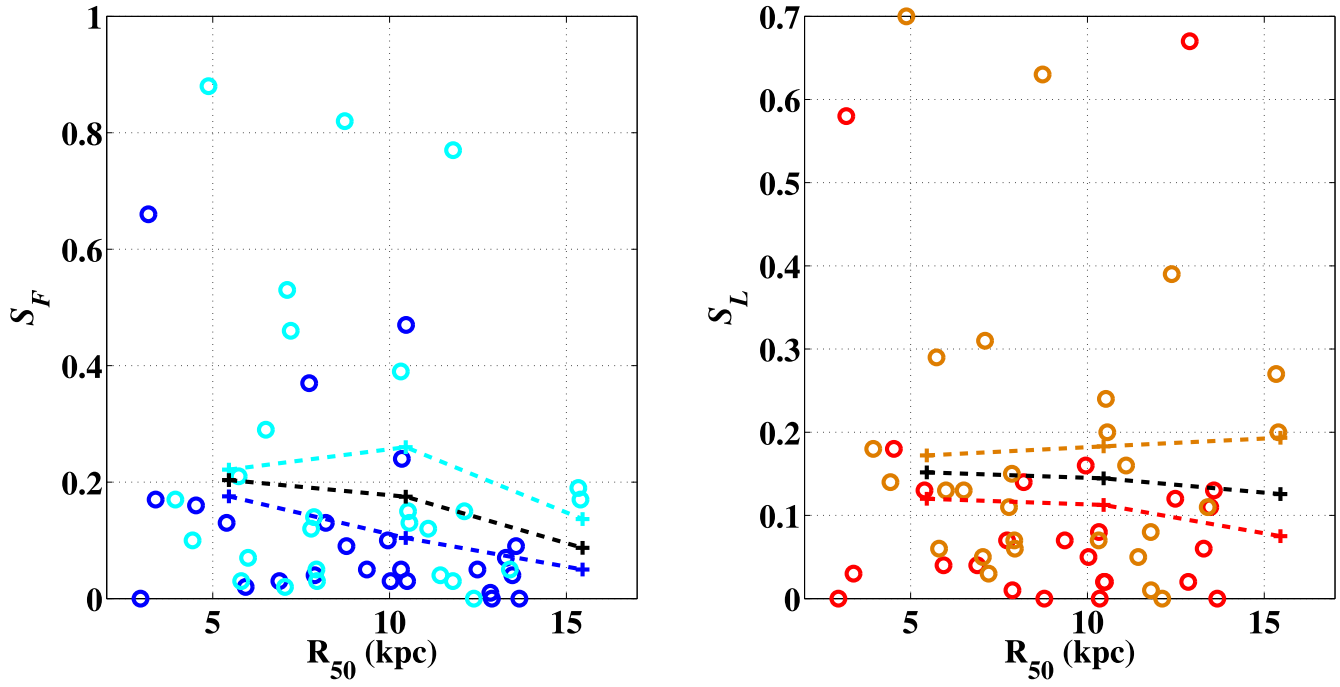

Figure 13. The relationships between the symmetry of galaxies and their R_{50} properties for mean values (shown by a +) of each bin (2.5, 7.5, etc.) for the FIRST and LoTSS data are demonstrated in the left and right scatter plots, respectively. The symbols are the same as those in Figure 6.

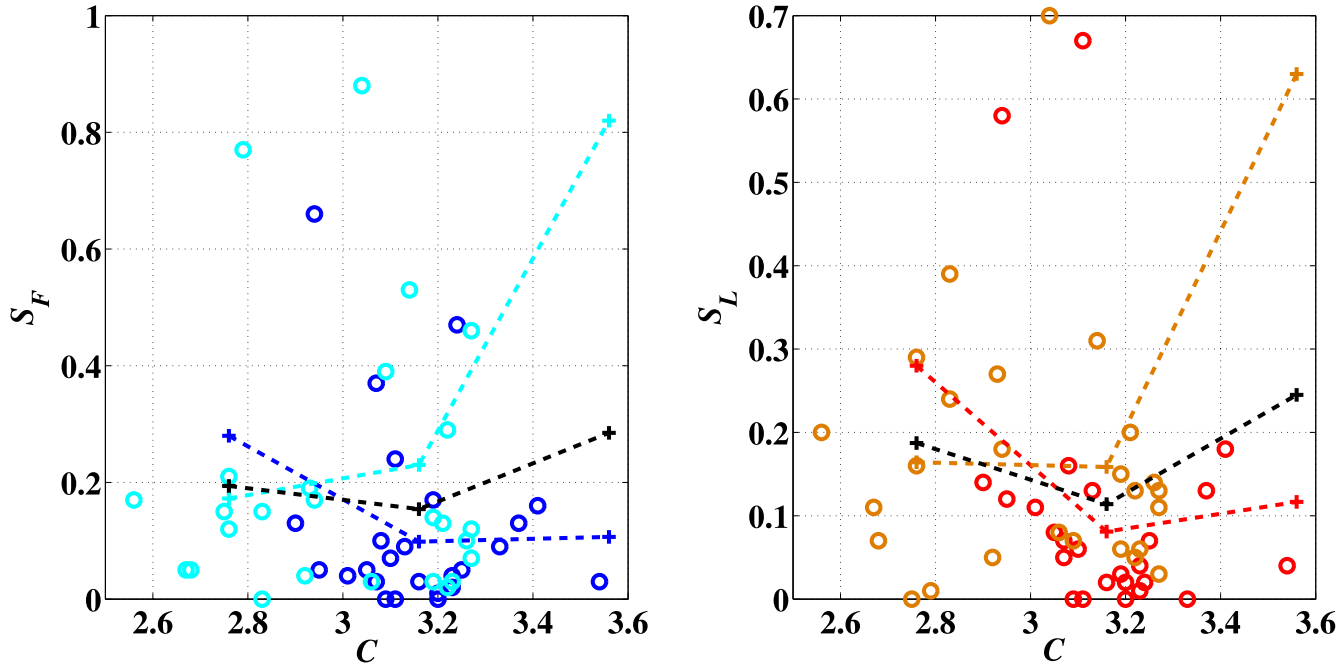

Figure 14. The relationships between the symmetry of galaxies and their concentrations for mean values (shown by a +) of each bin (2.55, 2.95, etc.) for the FIRST and LoTSS data are demonstrated in the left and right scatter plots, respectively. The symbols are the same as those in Figure 6.

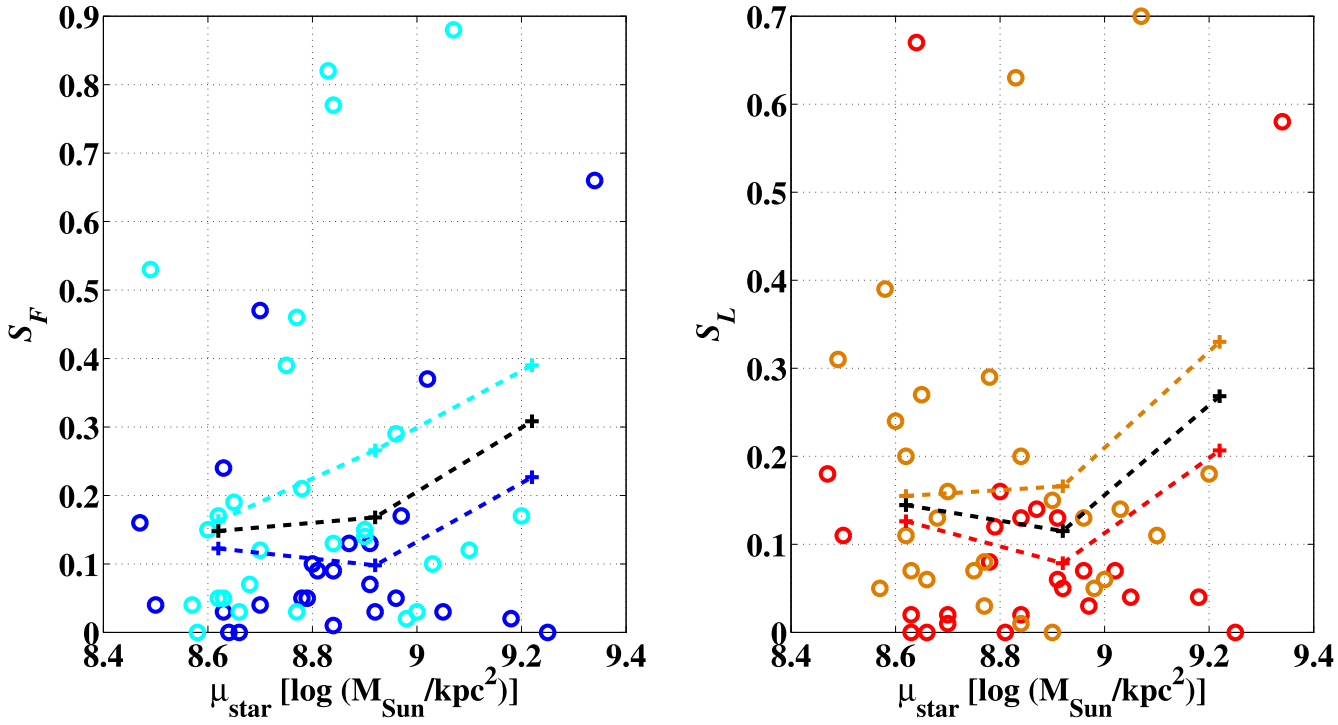

Figure 15. The relationships between the symmetry of galaxies and $\mu_{\rm star}$ for mean values (shown by a +) of each bin (8.45, 8.75, etc.) for the FIRST and LoTSS data are demonstrated in the left and right scatter plots, respectively. The symbols are the same as those in Figure 6.

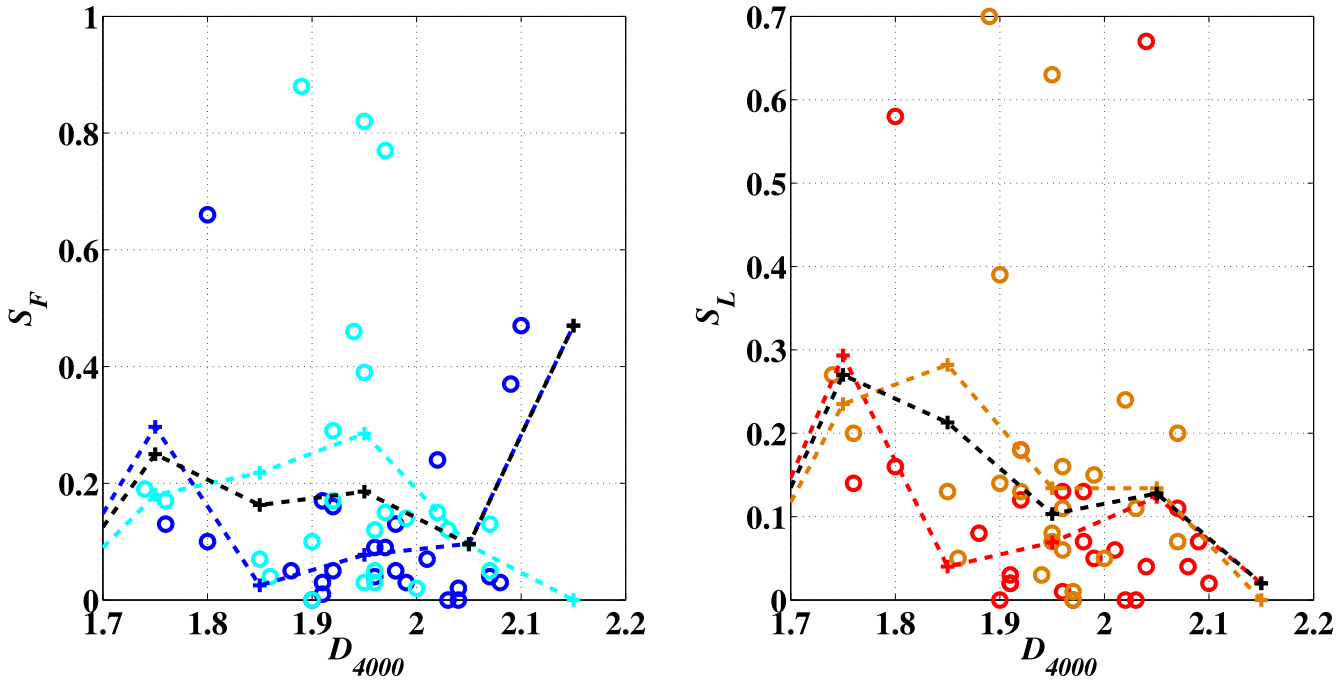

Figure 16. The relationships between the symmetry of galaxies and stars' ages for mean values (shown by a +) of each bin (1.7, 1.8, etc.) for the FIRST and LoTSS data are demonstrated in the left and right scatter plots, respectively. The symbols are the same as those in Figure 6.

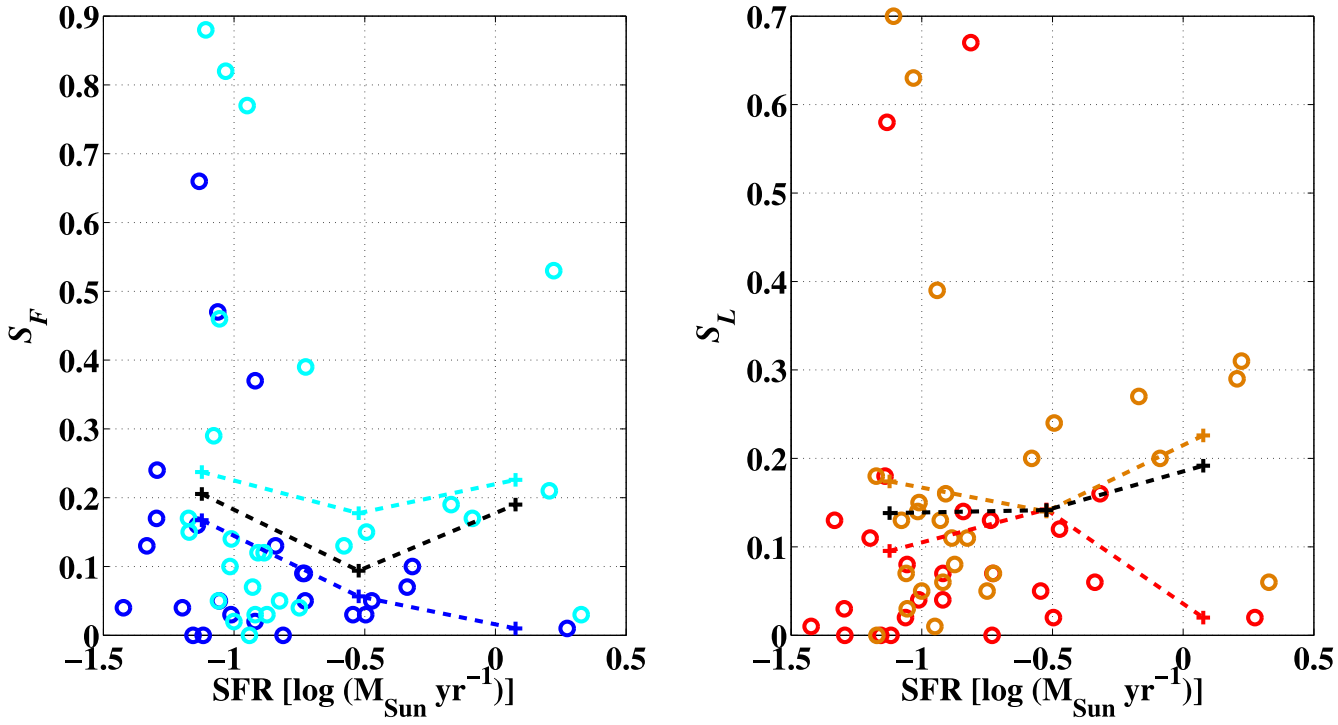

Figure 17. The relationships between the symmetry of galaxies and SFR for mean values (shown by a +) of each bin (−1.5, −0.9, etc.) for the FIRST and LoTSS data are demonstrated in the left and right scatter plots, respectively. The symbols are the same as those in Figure 6.

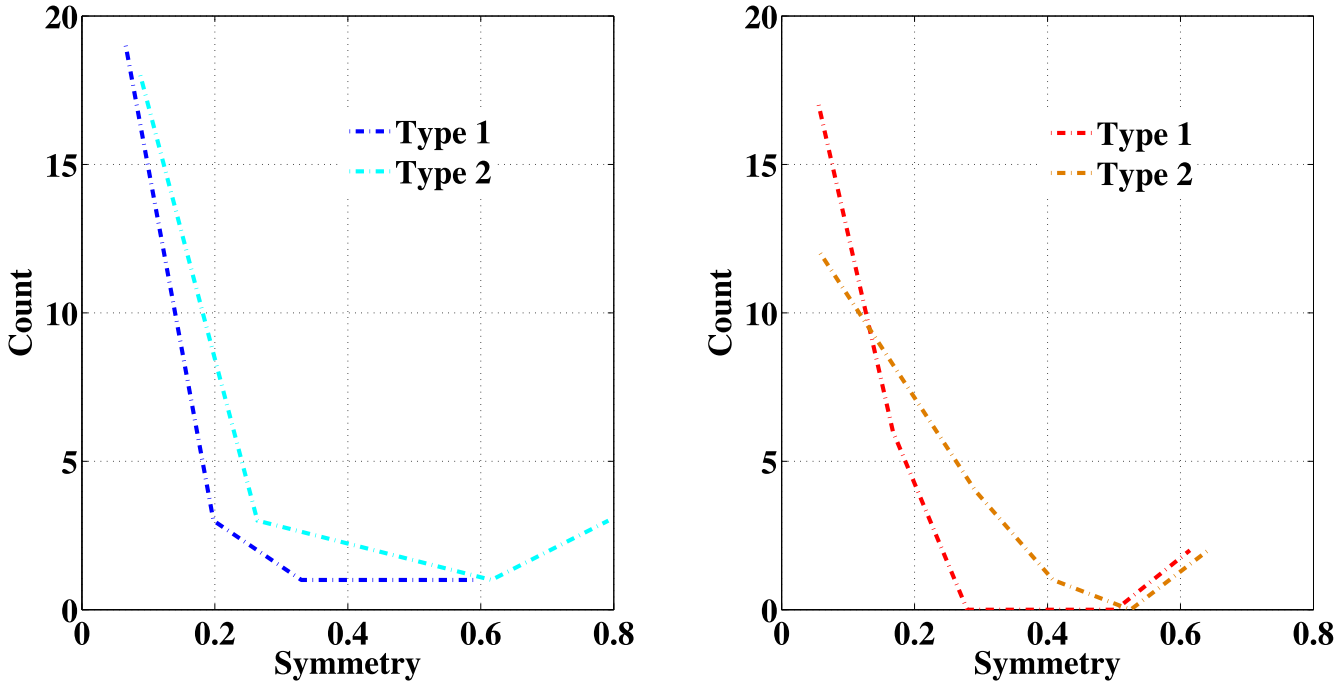

Figure 18. Distributions of symmetries for type I and type II galaxies in FIRST (left panel) and LoTSS (right panel) data sets.

Table 2
Median Values of Each Bin for Symmetries of the FIRST and LoTSS Data and Their Uncertainties

Figures	Type of Data Set	1st Bin	2nd Bin	3rd Bin	4th Bin	5th Bin
6	FIRST	0.11 ± 0.04	0.05 ± 0.02	0.04 ± 0.08	⋯	⋯
	LoTSS	0.13 ± 0.05	0.06 ± 0.02	0.04 ± 0.06	⋯	⋯
7	FIRST	0.12 ± 0.04	0.04 ± 0.03	0.03 ± 0.02	⋯	⋯
	LoTSS	0.13 ± 0.05	0.06 ± 0.06	0.02 ± 0.06	⋯	⋯
8	FIRST	0.13 ± 0.03	0.12 ± 0.07	0.04 ± 0.07	0	⋯
	LoTSS	0.11 ± 0.04	0.11 ± 0.04	0.05 ± 0.06	0	⋯
9	FIRST	0.08 ± 0.03	0.09 ± 0.03	0.17 ± 0.02	⋯	⋯
	LoTSS	0.10 ± 0.04	0.08 ± 0.04	0.12 ± 0.03	⋯	⋯
10	FIRST	0.10 ± 0.03	0.12 ± 0.03	0.04 ± 0.02	⋯	⋯
	LoTSS	0.07 ± 0.04	0.12 ± 0.04	0.05 ± 0.03	⋯	⋯
11	FIRST	0.17 ± 0.09	0.15 ± 0.01	0.13 ± 0.02	0.05 ± 0.03	0.12 ± 0.02
	LoTSS	0.11 ± 0.02	0.22 ± 0.02	0.10 ± 0.02	0.08 ± 0.03	0.07 ± 0.04
12	FIRST	0.16 ± 0.05	0.10 ± 0.02	0.05 ± 0.03	0.20 ± 0.02	⋯
	LoTSS	0.13 ± 0.03	0.08 ± 0.02	0.08 ± 0.04	0.07 ± 0.02	⋯
13	FIRST	0.13 ± 0.03	0.10 ± 0.03	0.07 ± 0.05	⋯	⋯
	LoTSS	0.11 ± 0.03	0.07 ± 0.03	0.11 ± 0.04	⋯	⋯
14	FIRST	0.15 ± 0.03	0.07 ± 0.03	0.15 ± 0.01	⋯	⋯
	LoTSS	0.16 ± 0.03	0.07 ± 0.04	0.16 ± 0.01	⋯	⋯
15	FIRST	0.06 ± 0.04	0.10 ± 0.03	0.15 ± 0.01	⋯	⋯
	LoTSS	0.10 ± 0.04	0.08 ± 0.05	0.15 ± 0.01	⋯	⋯
16	FIRST	0.31 ± 0.02	0.17 ± 0.03	0.15 ± 0.04	0.12 ± 0.03	0.05 ± 0.04
	LoTSS	0.22 ± 0.01	0.20 ± 0.02	0.13 ± 0.03	0.10 ± 0.03	0.07 ± 0.04
17	FIRST	0.12 ± 0.03	0.07 ± 0.04	0.18 ± 0.02	⋯	⋯
	LoTSS	0.10 ± 0.04	0.11 ± 0.03	0.24 ± 0.02	⋯	⋯

In addition to mean value of each bin displayed by "+" in all figures, we also computed medians to characterize the typical values of the symmetry distributions in each individual bin. Given the limited sample size and the small number of sources allocated to various bins, we employed the bootstrapping method (Efron & Tibshirani 1993) as one of the resampling approaches to find uncertainties associated with the medians. The results for all bins of Figures 6–17 are expressed in Table 2. In the majority of bins, the trends of the medians correspond with the means.

The three well-known correlation coefficients have been used to evaluate the confidence level of the correlations between symmetries of radio galaxies obtained from two catalogs and their physical parameters. Since the Pearson correlation is limited to Gaussian distributed data points, we provide the Spearman and Kendall correlations. Table 3 lists the different correlation coefficients in addition to the corresponding p-values for the total sample of radio galaxies. Similar results have been obtained when analyzing the data using Spearman and Kendall ranked correlation coefficients, as well as Pearson correlation. For the total sample of FR radio galaxies (back dotted line), the symmetry looks to be correlated with $\gtrsim$95% confidence to the radio size (Figures 6 and 7). Larger galaxies in radio size show smaller symmetry index. This is consistent with our expectation about symmetry. As far as we go to larger resolved sources, more detailed structures will appear in the map, breaking the symmetry. This result shows that the defined symmetry index is affected by the resolution of radio maps. The correlation is also presented for FRI and FRII in the left panels of Figures 6 and 7. Other properties do not show strong correlations with the symmetry except R_{50} for FRI in Figure 13, stellar age for the total galaxy sample in Figure 16 and 150 MHz luminosity for FRI in Figure 8.

The correlation between radio luminosity and symmetry can also be explained due to the size–luminosity relation. Larger sources show higher radio power. The R_{50}-, stellar age-symmetry correlation can also be biased by the size of sources. This should be examined using larger samples of radio galaxies fixed in radio size.

Table 3
Correlations with Their p-values Between Parameters of Galaxies and Their Symmetries for the Total Sample of Radio Galaxies

	Symmetry of FIRST data			Symmetry of LoTSS data		
Physical	Pearson	Spearman	Kendall	Pearson	Spearman	Kendall
Parameter	⋯	p-values	⋯	⋯	p-values	⋯
Size (arcsec)	0.27	−0.06	−0.07	−0.21	−0.51	−0.37
	0.05	0.68	0.45	0.14	<0.01	<0.01
Size (kpc)	0.33	−0.06	−0.06	0.19	−0.13	−0.09
	0.02	0.66	0.54	0.17	0.37	0.34
S (mJy)	−0.01	−0.06	−0.03	−0.09	−0.14	−0.09
	0.99	0.70	0.79	0.55	0.31	0.34
log[L/W (Hz^{-1})]	0.02	0.03	0.02	−0.06	−0.03	−0.01
	0.90	0.81	0.83	0.66	0.85	0.89
Redshift	−0.01	<0.01	−0.01	0.01	−0.01	−0.01
	0.96	0.99	0.98	0.94	0.95	0.93
Stellar mass [log($M_\odot$)]	−0.15	−0.20	−0.14	−0.14	−0.13	−0.07
	0.29	0.16	0.17	0.33	0.37	0.47
black hole mass [log($M_\odot$)]	−0.10	−0.18	−0.11	−0.18	−0.23	−0.15
	0.47	0.20	0.27	0.21	0.11	0.13
R_{50} (kpc)	−0.22	−0.23	−0.16	−0.09	−0.06	−0.04
	0.12	0.11	0.10	0.54	0.66	0.66
C	0.05	−0.08	−0.04	−0.04	−0.22	−0.16
	0.70	0.57	0.66	0.79	0.11	0.10
μ_{star} [log($M_\odot$/kpc^2)]	0.15	0.06	0.05	0.03	−0.12	−0.08
	0.28	0.67	0.60	0.83	0.41	0.42
D_{4000}	−0.18	−0.17	−0.12	−0.25	−0.34	−0.25
	0.19	0.24	0.23	0.08	0.01	0.01
SFR [log($M_\odot$/yr)]	−0.10	−0.13	−0.07	0.06	0.21	0.16
	0.48	0.35	0.49	0.68	0.13	0.10

Note. The top row for each physical parameter indicates the values of different types of correlations, and the bottom row displays their p-values.

4.2. Symmetry and FR Classification

The plots of the symmetry for FRI and FRII radio galaxies at 1.4 GHz and 150 MHz maps are shown in Figure 18. The median values of symmetries for the FRI and FRII are 0.05 ± 0.04 and 0.14 ± 0.02, respectively, in the FIRST data set. These values for the FRI and FRII are 0.06 ± 0.04 and 0.13 ± 0.04, respectively, in the LoTSS data set. The uncertainty values are computed by the bootstrapping method. FRIIs show higher symmetry than FRI radio galaxies. In Section 4.1, we demonstrated that the defined symmetry parameter is slightly correlated with the size of radio sources in our sample under consideration. In this section, we examine if higher symmetry observed in FRIIs is effected by this relation. In order to investigate this, we plot the radio size of FRI and FRII radio galaxies in Figure 19. The median values of radio sizes for the FRI and FRII are 57.47 ± 9.10 and 31.28 ± 7.20 arcsecs, respectively, in the FIRST data set. These values for the FRI and FRII are 116.08 ± 20.10 and 61.37 ± 12.04 arcsecs, respectively, in the LoTSS data set. The uncertainty values are computed by the bootstrapping method. FRIIs show lower radio size than FRIs. Therefore, the higher symmetry is expected. To remove the bias caused by size of sources, we need to make matched samples of FRI and FRII in size and then compare their symmetry indices.

In order to make a uniformly matched sample, we adopt four different methods:

i) We selected FRI/FRII pairs that were closest in size, with a difference in size of less than 30″. This method results in 15 unique pairs.
ii) We randomly matched an FRI with an FRII in size, with a difference in size of less than 30″. This method results in ∼20 unique pairs.

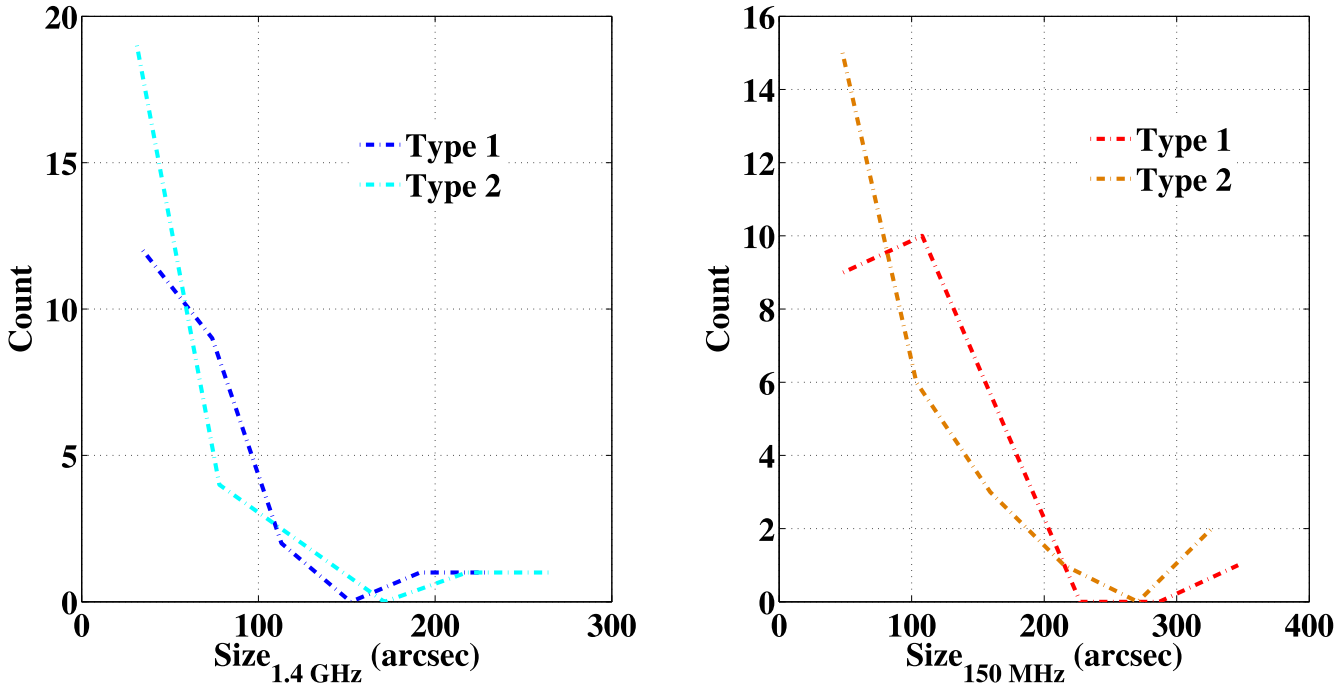

Figure 19. Distributions of sizes for type I and type II galaxies in FIRST (left panel) and LoTSS (right panel) data sets.

iii) We chose an FRI and found the closest FRII in size to join with the least size difference. This method results in 25 unique pairs.
iv) We chose an FRII and found the closest FRI in size to join with the least size difference. This method results in 26 unique pairs.

All four methods build similar distributions of FRI/FRII in radio sizes. Then, we compare the distributions of symmetry index for FRI/FRIIs. The confidence levels of differences have been estimated using the Kolmogorov–Smirnov test (Miraghaei 2020). For this aim, we make cumulative distributions of FRI/FRII matched samples normalized to unity and evaluate the maximum differences between the two samples to find the corresponding levels at which the null hypothesis is rejected. FRIIs in all subsamples show higher symmetry with the confidence levels of 85%, 90%, 97.5%, and 95% for methods i to iv, respectively. Therefore, the results of matched comparisons show that FRIIs have higher symmetry than FRIs. This result is not affected by the symmetry-size relation that we found in Section 4.1.

5. Conclusions

The current paper is the second one of our developing research on symmetry in radio galaxies. Paper I mostly includes description of data and definition of symmetry and related techniques. In this article (paper II), we dig more into the image segmentation process that involved intensity thresholding based on histogram analysis and the k-means clustering algorithm that performs grouping pixels with similar intensities into clusters based on mean distances. This allows for effective region extraction and morphological parameter derivation for symmetry definition.

We explained in detail a symmetry criterion (based on paper I) for different types of galaxies in various data sets. We explored the relationship between morphological symmetry in radio maps of galaxies and various properties of the host galaxy through scatter plots. The analysis is divided into two sets of properties: optical properties (such as stellar mass, black hole mass, R_{50}, concentration, μ_{50}, and stellar age) and radio properties (including radio flux density, radio luminosity, and radio size). We examined the total sample of radio galaxies as well as the FRI and FRII subsamples, plotting the symmetry parameter against other galaxy properties. The results show a correlation between symmetry and radio size, with larger galaxies displaying a smaller symmetry index. This correlation can be attributed to the resolution of the radio maps, as more detailed structures become visible in larger resolved sources, breaking the symmetry. Additionally, some weak correlations are observed between symmetry and other properties, such as R_{50} for FRI and stellar age for the total galaxy sample of FRI and FRII. We suggest that further examination using larger samples of radio galaxies, fixed in radio size, is needed to confirm these correlations.

Furthermore, we focused on the symmetry differences between FRI and FRII radio galaxies. We present a plot of

symmetry for FRI and FRII radio galaxies at 1.4 GHz and 150 MHz maps, showing that FRIIs exhibit higher symmetry compared to FRIs. To investigate if this higher symmetry is influenced by the size of radio sources, we plotted the radio size of FRI and FRII radio galaxies. It is observed that FRIIs have a lower radio size than FRIs, which explains the higher symmetry. To remove the size bias, four different methods of matching FRI and FRII samples in size are applied. The matched comparisons show that FRIIs consistently have higher symmetry than FRIs, independent of the symmetry-size relation. The results suggest that the higher symmetry observed in FRIIs is not solely influenced by the size of radio sources.

We emphasize the significant influence of the environment on shaping radio galaxies. Consequently, a crucial aspect of our investigation involves exploring the correlation between symmetry and the environment of these galaxies. Our findings highlight increased symmetry in FRII radio galaxies, underscoring the impact of the environment in disrupting the symmetry of radio sources. This observation is particularly noteworthy as FRIIs are consistently found in lower-density environments compared to FRIs. We make a preliminary report of our results. A larger sample would improve the outcome when it will be publicly available.

Our future investigation will focus on several aspects. First, each method is not perfect and can be improved by new ideas and definitions. Our definition of symmetry in the case of $\mathcal{S}_{\text{proximity}}$ is not invariant relative to scaling and may be made scale-invariant. Since the sources we work with have a consistent size of $5'$, the results are not affected by the definition of $\mathcal{S}_{\text{proximity}}$. Second, we aim to enhance the statistical analysis by utilizing a larger sample of radio galaxies. Third, we plan to explore the relationship between symmetry and the environments of these galaxies by incorporating appropriate parameters (Sabater et al. 2013) to characterize the host galaxy's environment. Lastly, we recognize the importance of refining the definition of symmetry for our future research endeavors.

Acknowledgments

The authors thank the reviewer for his/her very helpful and constructive comments and suggestions.

References

Abazajian, K. N., Adelman-McCarthy, J. K., Agüeros, M. A., et al. 2009, ApJS, 182, 543
Alegre, L., Sabater, J., Best, P., et al. 2022, MNRAS, 516, 4716
An, F. X., Stach, S. M., Smail, I., et al. 2018, ApJ, 862, 101
Aniyan, A. K., & Thorat, K. 2017, ApJS, 230, 20
Arshakian, T. G., & Longair, M. S. 2000, MNRAS, 311, 846
Augusto, P., Gonzalez-Serrano, J. I., Perez-Fournon, I., & Wilkinson, P. N. 2006, MNRAS, 368, 1411
Baldi, R. D., Capetti, A., & Giovannini, G. 2015, A&A, 576, A38
Balogh, M. L., Morris, S. L., Yee, H., Carlberg, R., & Ellingson, E. 1999, ApJ, 527, 54
Banhatti, D. G. 1980, A&A, 84, 112
Barkus, B., Croston, J. H., Piotrowska, J., et al. 2022, MNRAS, 509, 1
Baum, S. A., Zirbel, E. L., & O'Dea, C. P. 1995, ApJ, 451, 88
Becker, R. H., White, R. L., & Helfand, D. J. 1995, ApJ, 450, 559
Bera, S., Pal, S., Sasmal, T. K., & Mondal, S. 2020, ApJS, 251, 9
Best, P. N., Longair, M. S., & Roettgering, H. J. A. 1997, MNRAS, 292, 758
Bîrzan, L., McNamara, B. R., Nulsen, P. E. J., Carilli, C. L., & Wise, M. W. 2008, ApJ, 686, 859
Blanton, E. L., Gregg, M. D., Helfand, D. J., Becker, R. H., & Leighly, K. M. 2001, AJ, 121, 2915
Blanton, E. L., Gregg, M. D., Helfand, D. J., Becker, R. H., & White, R. L. 2000, ApJ, 531, 118
Bridle, A. H., Hough, D. H., Lonsdale, C. J., Burns, J. O., & Laing, R. A. 1994, AJ, 108, 766
Brinchmann, J., Charlot, S., White, S. D. M., et al. 2004, MNRAS, 351, 1151
Cegłowski, M., Gawroński, M. P., & Kunert-Bajraszewska, M. 2013, A&A, 557, A75
Chibueze, J. O., Sakemi, H., Ohmura, T., et al. 2021, Natur, 593, 47
Condon, J. J. 1992, ARA&A, 30, 575
Condon, J. J., Cotton, W. D., Greisen, E. W., et al. 1998, AJ, 115, 1693
Cornwell, T. J., Saikia, D. J., Shastri, P., et al. 1986, JApA, 7, 119
Das, B., Chandra, P., Shultz, M. E., et al. 2022, MNRAS, 517, 5756
de Gasperin, F., Rudnick, L., Finoguenov, A., et al. 2022, A&A, 659, A146
Dehghan, S., Johnston-Hollitt, M., Franzen, T. M. O., Norris, R. P., & Miller, N. A. 2014, AJ, 148, 75
Dennett-Thorpe, J., Bridle, A. H., Laing, R. A., & Scheuer, P. A. G. 1999, MNRAS, 304, 271
Donoho, D. L., & Johnstone, I. M. 1994, Biometrika, 81, 425
Efron, B., & Tibshirani, R. J. 1993, An Introduction to the Bootstrap, Monographs on Statistics and Applied Probability No. 57 (Boca Raton, FL: Chapman & Hall/CRC)
Fanaroff, B. L., & Riley, J. M. 1974, MNRAS, 167, 31P
Gawroński, M. P., Marecki, A., Kunert-Bajraszewska, M., & Kus, A. J. 2006, A&A, 447, 63
Gendre, M. A., Best, P. N., & Wall, J. V. 2010, MNRAS, 404, 1719
Gendre, M. A., Best, P. N., Wall, J. V., & Ker, L. M. 2013, MNRAS, 430, 3086
Gopal-Krishna, & Wiita, P. J. 2000, A&A, 363, 507
Gopal-Krishna, & Wiita, P. J. 2002, New Astron. Rev., 46, 357
Gupta, V., Mahle, R., & Shriwas, R. S. 2013, Image denoising using wavelet transform method in 2013 Tenth Int. Conf. on Wireless and Optical Communications Networks (WOCN) *(Bhopal, India, 26-28 July 2013)* (IEEE) 1, 2151-7703
Hajdukovic, D. S. 2010, EL, 89, 49001
Hardcastle, M., & Croston, J. 2020, NewAR, 88, 101539
Hardcastle, M. J., Sakelliou, I., & Worrall, D. M. 2005, MNRAS, 359, 1007
Harwood, J. J., Vernstrom, T., & Stroe, A. 2020, MNRAS, 491, 803
Heckman, T. M., & Best, P. N. 2014, ARA&A, 52, 589
Hill, G. J., & Lilly, S. J. 1991, ApJ, 367, 1
Hocuk, S., & Barthel, P. D. 2010, A&A, 523, A9
Javaherian, M., Miraghaei, H., & Moradpour, H. 2023, AJ, 166, 124
Jimenez-Gallardo, A., Massaro, F., Capetti, A., et al. 2019, A&A, 627, A108
Kauffmann, G., Heckman, T. M., White, S. D. M., et al. 2003a, MNRAS, 341, 33
Kauffmann, G., Heckman, T. M., White, S. D. M., et al. 2003b, MNRAS, 341, 54
Kauffmann, G., Heckman, T. M., Tremonti, C., et al. 2003c, MNRAS, 346, 1055
Kornreich, D. A., Haynes, M. P., & Lovelace, R. V. E. 1998, AJ, 116, 2154
Kravtsov, A. V., & Borgani, S. 2012, ARA&A, 50, 353
Laing, R. A., Parma, P., de Ruiter, H. R., & Fanti, R. 1999, MNRAS, 306, 513
Lara, L., Giovannini, G., Cotton, W. D., et al. 2004, A&A, 421, 899
Longair, M. S. 2011, High Energy Astrophysics (3rd ed.; Cambridge: Cambridge Univ. Press)
Lukic, V., Brüggen, M., Banfield, J. K., et al. 2018, MNRAS, 476, 246
Mantovani, F., Fanti, R., Ferrari, C., Cotton, W., & Muxlow, T. W. B. 2003, A&A, 399, 449
Mazharimousavi, S. H., Halilsoy, M., Sakalli, I., & Gurtug, O. 2010, CQGra, 27, 105005
Mazoochi, F., Miraghaei, H., & Riazi, N. 2022, PASA, 39, e021

McCarthy, P. J., van Breugel, W., Spinrad, H., & Djorgovski, S. 1987, ApJL, 321, L29
Mingo, B., Croston, J. H., Hardcastle, M. J., et al. 2019, MNRAS, 488, 2701
Miraghaei, H. 2020, Astron. J, 160, 227
Miraghaei, H., & Best, P. N. 2017, MNRAS, 466, 4346
Mo, H., van den Bosch, F., & White, S. 2010, Galaxy Formation and Evolution (Cambridge: Cambridge Univ. Press)
Morganti, R., Tadhunter, C. N., Oosterloo, T. A., et al. 2003, PASA, 20, 129
Noori, M., Javaherian, M., Safari, H., & Nadjari, H. 2019, AdSpR, 64, 504
O'Brien, A. N., Tothill, N. F. H., Norris, R. P., & Filipović, M. D. 2015, Proc. of "The Many Facets of Extragalactic Radio Surveys: Towards New Scientific Challenges"
O'Dea, C. P., & Saikia, D. J. 2021, A&ARv, 29, 3
Pacholczyk, A. 1970, Radio Astrophysics: Nonthermal Processes in Galactic and Extragalactic Sources, Astronomy and Astrophysics Series (San Francisco, CA: W. H. Freeman)
Podigachoski, P., Barthel, P., Haas, M., Leipski, C., & Wilkes, B. 2015, ApJL, 806, L11
Pérez-Torres, M.-A., & De Breuck, C. 2005, MNRAS, 363, L41
Readhead, A. C. S., Taylor, G. B., Xu, W., et al. 1996, ApJ, 460, 612
Rys, S. 1994, A&A, 281, 15
Sabater, J., Best, P. N., & Argudo-Fernández, M. 2013, MNRAS, 430, 638
Sadeghi, M., Javaherian, M., & Miraghaei, H. 2021, AJ, 161, 94
Saikia, D. J., Jeyakumar, S., Mantovani, F., et al. 2003, PASA, 20, 50
Saikia, D. J., Shastri, P., Sinha, R. P., Kapahi, V. K., & Swarup, G. 1984, JApA, 5, 429
Sarazin, C. L. 1988, X-ray Emission from Clusters of Galaxies (Cambridge: Cambridge Univ. Press)
Sarzi, M., Falcón-Barroso, J., Davies, R. L., et al. 2006, MNRAS, 366, 1151
Schweizer, F. 1997, in Proc. of the 186th Symp. of the International Astronomical Union: Galaxy Interactions at Low and High Redshift, ed. J. E. Barnes & D. B. Sanders (Dordrecht: Springer)
Shen, S., Mo, H. J., White, S. D. M., et al. 2003, MNRAS, 343, 978
Shimazaki, H., & Shinomoto, S. 2007, neco, 19, 1503
Shimwell, T. W., Röttgering, H. J. A., Best, P. N., et al. 2017, A&A, 598, A104
Shimwell, T. W., Tasse, C., Hardcastle, M. J., et al. 2019, A&A, 622, A1
Sparke, L. S., & Gallagher, J. S., III 2007, Galaxies in the Universe: An Introduction (Cambridge: Cambridge Univ. Press)
Stahler, S. W., & Palla, F. 2004, The Formation of Stars (New York: Wiley)
Strateva, I., Ivezić, Ž., Knapp, G. ., et al. 2001, AJ, 122, 1861
Tadhunter, C. 2007, NewAR, 51, 153
Tajik, Z., Javaherian, M., Daei, F., et al. 2023, AdSpR, 72, 1884
Tang, H., Scaife, A. M. M., & Leahy, J. P. 2019, MNRAS, 488, 3358
Taylor, G. B., Readhead, A. C. S., & Pearson, T. J. 1996a, ApJ, 463, 95
Taylor, G. B., Vermeulen, R. C., Readhead, A. C. S., et al. 1996b, ApJS, 107, 37
Taylor, M. B. 2005, in ASP Conf. Ser. 347, Astronomical Data Analysis Software and Systems XIV, ed. P. Shopbell, M. Britton, & R. Ebert (San Francisco, CA: ASP), 29
Tremaine, S., Gebhardt, K., Bender, R., et al. 2002, ApJ, 574, 740
van Haarlem, M. P., Wise, M. W., Gunst, A. W., et al. 2013, A&A, 556, A2
Vikhlinin, A., Kravtsov, A., Forman, W., et al. 2006, ApJ, 640, 691
Williams, W. L., Hardcastle, M. J., Best, P. N., et al. 2019, A&A, 622, A2
Wolter, A., Caccianiga, A., della Ceca, R., & Maccacaro, T. 1994, ApJ, 433, 29
York, D. G., Adelman, J., Anderson, J. E. J., et al. 2000, AJ, 120, 1579
Yousefzadeh, M., Javaherian, M., & Safari, H. 2015, IJAA, 2, 69
Yuan, F., & Narayan, R. 2014, ARA&A, 52, 529